Photoacoustics 43 (2025) 100721

Contents lists available at ScienceDirect

Photoacoustics

journal homepage: www.elsevier.com/locate/pacs

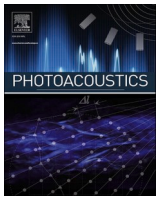

Dual-modality ultrasound/photoacoustic tomography for mapping tissue oxygen saturation distribution in intestinal strangulation

Jie Zhou [a,1], Mengchuan Ou [b,1], Bo Yuan [b], Binzi Yan [a], Xichuan Wang [c], Shuaiqi Qiao [d], Yijie Huang [d], Lian Feng [a], Lin Huang [d,*], Yan Luo [a,*]

[a] Ultrasound department of West China Hospital of Sichuan University, Chengdu, Sichuan 610041, China
[b] General surgery department of the Sixth People's Hospital of Chengdu, Sichuan 610000, China
[c] Pathology department of the Sixth People's Hospital of Chengdu, Sichuan 610000, China
[d] School of Electronic Science and Engineering, University of Electronic Science and Technology, Chengdu, Sichuan 611731, China

ARTICLE INFO

Keywords:
Dual-modality ultrasound/photoacoustic tomography imaging
Photoacoustic tomography
Simple intestinal obstruction
Strangulated intestinal obstruction
Oxygen saturation

ABSTRACT

The strangulation of intestinal obstruction (IO) presents challenges in the assessment of disease progression and surgical decision-making. Intraoperatively, an accurate evaluation of the status of the IO is critical for determining the extent of surgical resection. Dual-modality ultrasound/photoacoustic tomography (US/PAT) imaging has the potential to provide spatially resolved tissue oxygen saturation (SO_2), serving as a valuable marker for IO diagnosis. In this study, US/PAT was utilized for imaging rat models of IO, with the data used for reconstruction, statistical analysis, and distribution evaluation. Results showed that SO_2 decreased with increasing strangulation severity. Notably, the kurtosis and skewness of the SO_2 distribution outperformed SO_2 itself in diagnosis, as they more effectively capture the heterogeneity of SO_2 distribution. Kurtosis reflects distribution concentration, while skewness measures asymmetry, both achieving areas under the receiver operating characteristic curve (AUROC) of 0.969. In conclusion, US/PAT offers a rapid and convenient method for assessing strangulation in IO.

1. Introduction

Intestinal obstruction (IO) is a common surgical emergency that often requires immediate surgical intervention, with high rates of missed or incorrect diagnoses. IO accounts for 20 % of acute abdominal surgical cases and has a mortality rate of up to 10 % [1]. Based on whether blood flow is compromised, IO can be classified into simple intestinal obstruction (Sim-IO) and strangulated intestinal obstruction (Str-IO). Str-IO is the more severe condition, and if left untreated or delayed, it can result in serious complications such as peritonitis, infection and toxic shock, with mortality rates reaching as high as 30 % [2]. At this stage, prompt surgical resection of the affected segment is warranted. Accurate diagnosis and the timely initiation are therefore critical to achieving positive outcomes. Developing a better method to distinguish Sim-IO from the more urgent Str-IO is an essential goal.

To evaluate intestinal status, surgeons use various modalities preoperatively and intraoperatively. The primary diagnostic method depends on the surgeon's subjective assessment of preoperative symptoms and signs of peritonitis, along with intraoperative evaluations of intestinal appearance and motility, et al. Supplementary diagnostic tools, such as computed tomography (CT), are commonly used in clinical practice for preoperative diagnosis and assessment of intestinal obstruction and related complications [3]. However, early signs of IO are often subtle, and the disease evolves dynamically. While CT can capture immediate findings, it is limited in tracking the progression of IO. Additionally, critically ill patients may not tolerate transport for CT, and it is unsuitable for intraoperative use. Contrast-enhanced ultrasound (CEUS) has emerged as a valuable tool for visualizing microvasculature and assessing vascular patency in affected bowel segments [4]. However, limited data compare CEUS findings with histology in IO, highlighting the need for further research [4]. So far, despite extensive research, no standardized method exists due to the complexity, limited reproducibility, and high costs of these modalities. Intraoperative assessments are typically subjective, highlighting the need for objective tools to enable a more accurate and comprehensive evaluation of intestinal status.

The photoacoustic (PA) effect refers to the generation of acoustic waves when an object is illuminated by pulsed or intensity-modulated

* Corresponding authors.
E-mail addresses: lhuang@uestc.edu.cn (L. Huang), yanluo@scu.edu.cn (Y. Luo).
[1] Co-first author

https://doi.org/10.1016/j.pacs.2025.100721
Received 9 February 2025; Accepted 31 March 2025
Available online 1 April 2025

continuous-wave electromagnetic waves, particularly light [5]. At the microscopic level, photons penetrate tissue and are absorbed by biomolecules such as hemoglobin, DNA/RNA, lipids, and melanin through electronic or vibrational absorption [6–8]. This absorbed energy is converted into heat via nonradiative relaxation. At the macroscopic level, the heat induces pressure waves that propagate through tissue as ultrasound. These waves are detected by transducers to create images that represent the optical energy distribution in the tissue [9–11] (Fig. 1). This phenomenon forms the basis of photoacoustic imaging, a hybrid modality combining the high contrast of optical imaging with the superior spatial resolution of ultrasound [12]. Photoacoustic tomography (PAT) uses pulsed laser beams to uniformly illuminate tissue and generate acoustic pulse responses. Ultrasound transducers then detect these signals, which are amplified and reconstructed into tomography images using computer algorithms. Additionally, PA can quantify tissue oxygen saturation (SO_2) by measuring the concentrations of deoxygenated hemoglobin (HB) and oxygenated hemoglobin (HBO_2), providing a safe, efficient, and cost-effective method for assessing SO_2.

Over the past two decades, PA imaging has evolved into a powerful diagnostic tool, demonstrating particular strength in intestinal imaging through its non-invasive capacity to quantify hemoglobin levels and SO_2 - biomarkers critical for both foundational research and clinical applications in disease diagnosis and treatment [13]. For instance, PA can assess vascular heterogeneity and hypoxia in gastrointestinal tumors [14], evaluate the activity of inflammatory bowel diseases such as Crohn's disease [15] and colitis [16,17], monitor various functional parameters of the gastrointestinal tract [18], and evaluate the degree of intestinal ischemia and hypoxia [19,20]. A representative study by Wang et al. established its diagnostic potential through real-time monitoring of intestinal ischemia-reperfusion injury in rat models [19]. The results showed that the levels of PA parameters, including HBO_2, HB, and PA amplitude at 760 nm and 840 nm, were significantly elevated in the ischemia groups, particularly in the 2-hour ischemia group, compared to the control group ($P < 0.05$). Furthermore, prolonged ischemia time exacerbated the injury. However, PA or PAT is limited by its spatial resolution. The analysis of the region of interest relies on PA images, which cannot clearly define the structural details and boundaries.

The combination of ultrasound (US) and PAT, known as dual-modality US/PAT imaging, addresses this limitation by integrating tissue localization from US with functional data from PAT, such as oxygen saturation, to produce functional images with precise spatial location. For instance, Sugiura et al. utilized the PA system (Vevo LAZR/2100 imaging system), which overlays oxygenation maps on US images [20]. Their study demonstrated the prediction of intestinal viability through consecutive photoacoustic monitoring of oxygenation recovery following reperfusion in the rat model of acute mesenteric ischemia. Their results showed a significant negative correlation between oxygenation and pathological severity, indicating that the combination of PA and US can objectively predict irreversible ischemic damage immediately after reperfusion, potentially guiding more accurate surgical decisions.

Recently, the diagnostic potential of dual-modality US/PAT imaging for differentiating Sim-IO from Str-IO has not been fully explored. This study developed rat models of IO to simulate the pathophysiological changes seen in humans with acute bowel obstruction or strangulated hernia. After conducting dual-modality US/PAT imaging for IO, a comparative analysis was performed with CEUS findings, laboratory results, and pathological examinations. The effectiveness of these imaging modalities in distinguishing between strangulated and simple IO was evaluated.

2. Methods

2.1. Animals and modeling

All animal procedures were conducted in strict accordance with the National Institutes of Health guidelines for the Care and Use of Laboratory Animals and were approved by the Institutional Animal Care and Use Committee of The Sixth People's Hospital of Chengdu (License Number: 2021-k-015). Male Sprague-Dawley rats, 8 weeks old and weighing 280 ± 20 g, were randomly assigned to Control (sham-operation), Sim-IO, and Str-IO groups. Before surgery, the rats underwent a 12-hour fast with free access to water. Anesthesia was induced using Zoletil® 50 (60 mg/kg), and body temperature was maintained at 37°C with a heating pad. The animal modeling procedure is shown in Fig. 2. After preparing and disinfecting the abdominal skin, a 2 cm longitudinal incision was made in the lower abdomen. The skin and muscle layers were carefully separated to create a subcutaneous space to accommodate a segment of the intestine. During laparotomy, the terminal ileum, approximately 4 cm proximal to the ileocecal junction, was isolated and translocated into the subcutaneous space. The mesentery was fixed to the abdominal wall musculature to stabilize the intestinal segment, and the abdominal muscle layer was closed without exerting pressure on the isolated intestinal segment or its mesentery. The subcutaneous space was gently compressed with gauze to expel air, and liquid paraffin oil

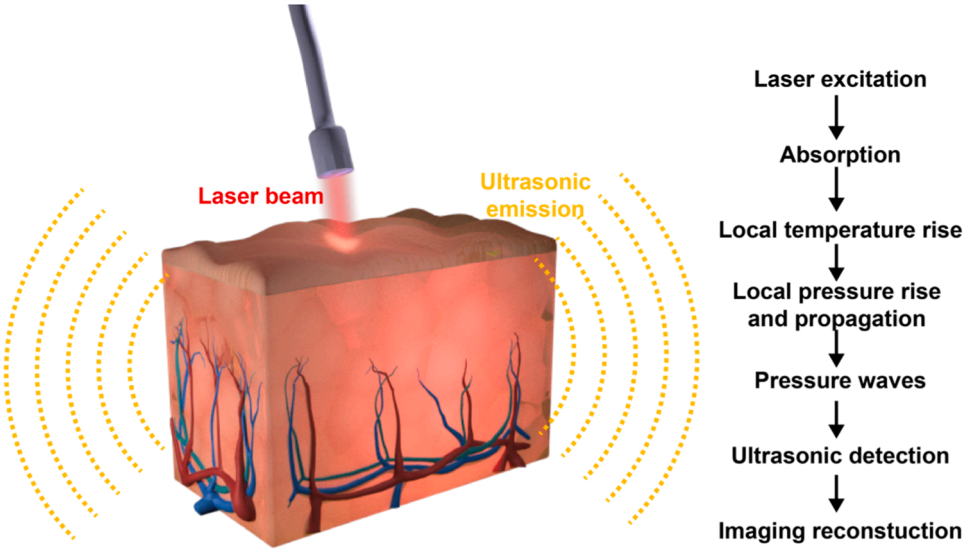

Fig. 1. Schematic diagram of the photoacoustic imaging principles.

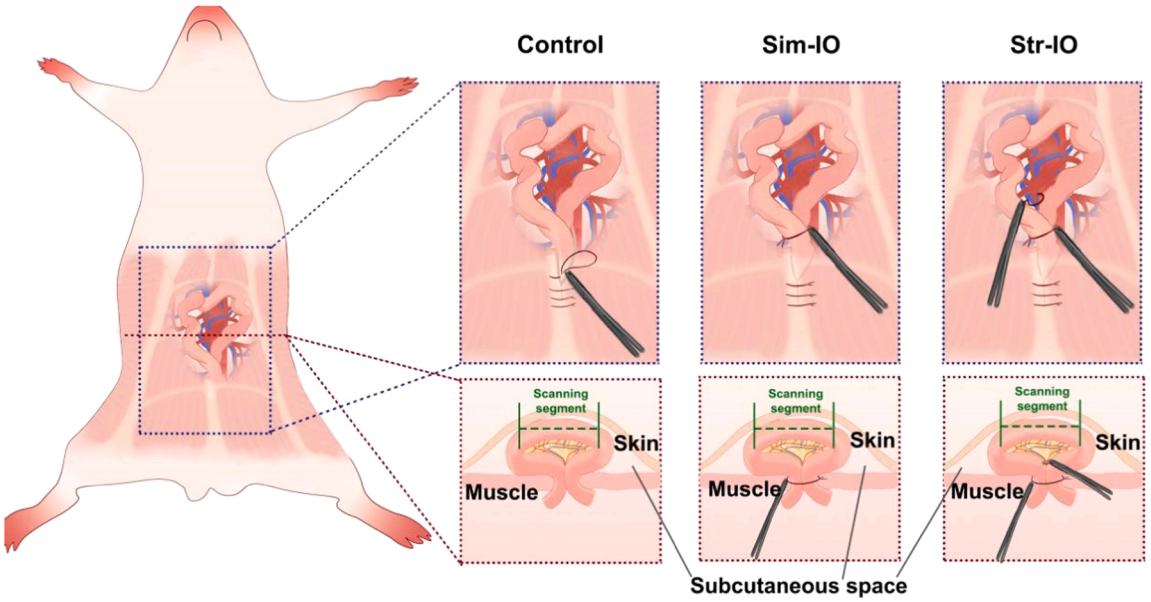

Fig. 2. Schematic diagram of rat IO models: control (sham operation group), simple intestinal obstruction (Sim-IO), and strangulated intestinal obstruction (Str-IO) groups. Note: The green dashed line represents the region for scanning and imaging of the dual-modality US/PAT imaging.

was added as needed. Finally, the skin was sutured continuously. In the Sim-IO group, the intestinal loop in the hernia ring was ligated with sutures, but the mesenteric vessels were left intact. In the Str-IO group, the entire intestinal loop was ligated, including the mesenteric vessels. Dual-modality US/PAT was performed one hour after surgery. Before dual-modality US/PAT, liquid paraffin oil was injected into the

A

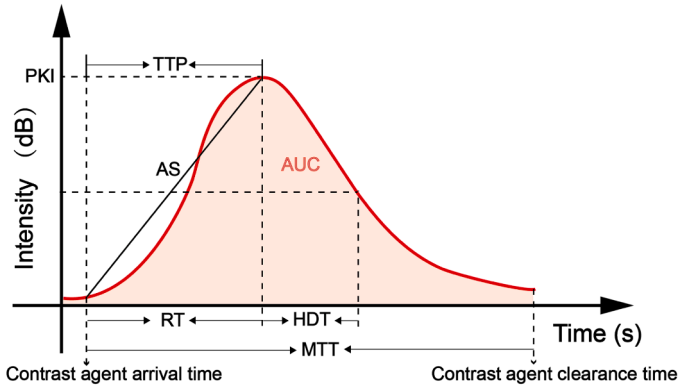

B

CEUS parameters	Significances
Peak intensity (PKI)	PKI refers to the maximum value of the contrast agent strength at the highest point of the curve
Area under curve (AUC)	The AUC represents the integral of the contrast agent intensity from baseline to enhancement.
Time to peak (TTP)	The time interval from the initiation of contrast agent injection to the moment it reaches peak intensity is referred to as the TTP.
Half-peak decline time (HDT)	The interval from the moment the contrast agent reaches its peak intensity to the point at which its intensity decreases to half of that peak, referred to as the HDT.
Mean transition time (MTT)	The interval between the point at which the contrast agent reaches and the subsequent clearance of the agent is known as the time to clearance.
Rising time (RT)	The interval from the moment the contrast agent arrives at the site to the point at which it reaches peak intensity is an important parameter in assessing the agent's distribution and effectiveness.
Ascending slope (AS)	The change in intensity, calculated by subtracting the initial intensity from the peak intensity and then dividing by the rise time.

Fig. 3. Illustration and significance of CEUS characteristic parameters. (A) Schematic representation of CEUS characteristic parameters, with corresponding abbreviations listed in the table below. (B) Significance of CEUS characteristic parameters.

intestinal cavity via a syringe in the subcutaneous space to eliminate gas interference.

2.2. CEUS examination

To mitigate the effects of ultrasound contrast agents on dual-modality US/PAT, additional animals were selected in each group for modeling and CEUS examinations. The contrast agent used was SonoVue (Bracco, Italy). According to the manufacturer's instructions, the lyophilized SonoVue powder was dissolved in 5 mL of saline. The injection dosage was determined based on the recommended human dose (2.0 mL for a 50 kg person) and adjusted according to the rats' body weight to ensure consistent enhancement across individual subjects. After intravenous injection of the contrast agent via the tail vein, a small saline flush was administered. CEUS imaging was performed using the Philips iU22 ultrasound system (Philips Medical Systems, Netherlands) with a low mechanical index (MI) microbubble imaging mode, utilizing an L8–3 MHz transducer. The transducer was fixed over the subcutaneously secured intestinal region, and a coupling agent was applied to eliminate gas interference. Immediately after the contrast agent injection, the built-in video recording mode was activated, capturing 120 seconds of DICOM video. For analysis, 2 mm^2 regions of interest (ROI) were selected for each animal, and time-intensity curve calculations were conducted to obtain key parameters, including peak intensity (PKI), area under the curve (AUC), time to peak (TTP), half-peak decline time (HDT), mean transit time (MTT), rise time (RT), and ascending slope (AS). The definitions of these CEUS parameters are illustrated in Fig. 3.

2.3. US/PAT system and data acquisition

As illustrated in Fig. 4A, the PAT system included a Q-switched Nd:YAG pumped optical parametric oscillator (Surelite, Continuum, California) for illumination in the 700–960 nm range, a linear fiber array (LFA) providing line-shaped illumination with dimensions of 40 mm × 10 mm (long axis × short axis), and a 128-element linear ultrasonic transducer array (Sesat Technology Co., Ltd.) with a central frequency of 8.5 MHz. A precision stepper motor (TSA100-B, Beijing Zolix Instrument Co., Ltd., China) provided micron-level accuracy. The collected signals were transmitted to a data acquisition system (DAQ) through an integrated amplifier (voltage gain: 1–80 dB; −3 dB bandwidth: 20 kHz to 10 MHz; Marsonics DAQ, Tianjin Langyuan Technology Co., Ltd., China) and digitized at a sampling rate of 40 million samples per second (Msps). The digitized data were transferred to a computer for imaging, real-time visual feedback, and storage for further analysis.

Dual-modality US/PAT scanning is performed using a precisely controlled stepping motor. The scanning start and end positions are predetermined and recorded. The motor operates at a frequency of 5 Hz with a step size of 1 mm. Each US or PAT scanning session lasts 5 seconds, covering the subcutaneous intestinal segment (Please refer to the green dashed portion depicted in the cross-sectional view of Schematic Fig. 2.

For PAT imaging, two wavelengths (780 nm and 820 nm) are used. Their close proximity ensures similar tissue absorption characteristics, improving the accuracy of SO_2 measurements and reducing errors from external factors. Additionally, the laser provides a stable energy output near 800 nm, making 780 nm and 820 nm ideal for the scanning process.

To prevent movement during scanning, the obstructed bowel segment was fixed in the subcutaneous space, with the mesentery sutured to the abdominal musculature. The space was filled with liquid paraffin oil to stabilize the target. Rats were placed on a secure platform with immobilized limbs to minimize respiratory motion. A degassed, transparent ultrasonic coupling agent was applied between the dual-

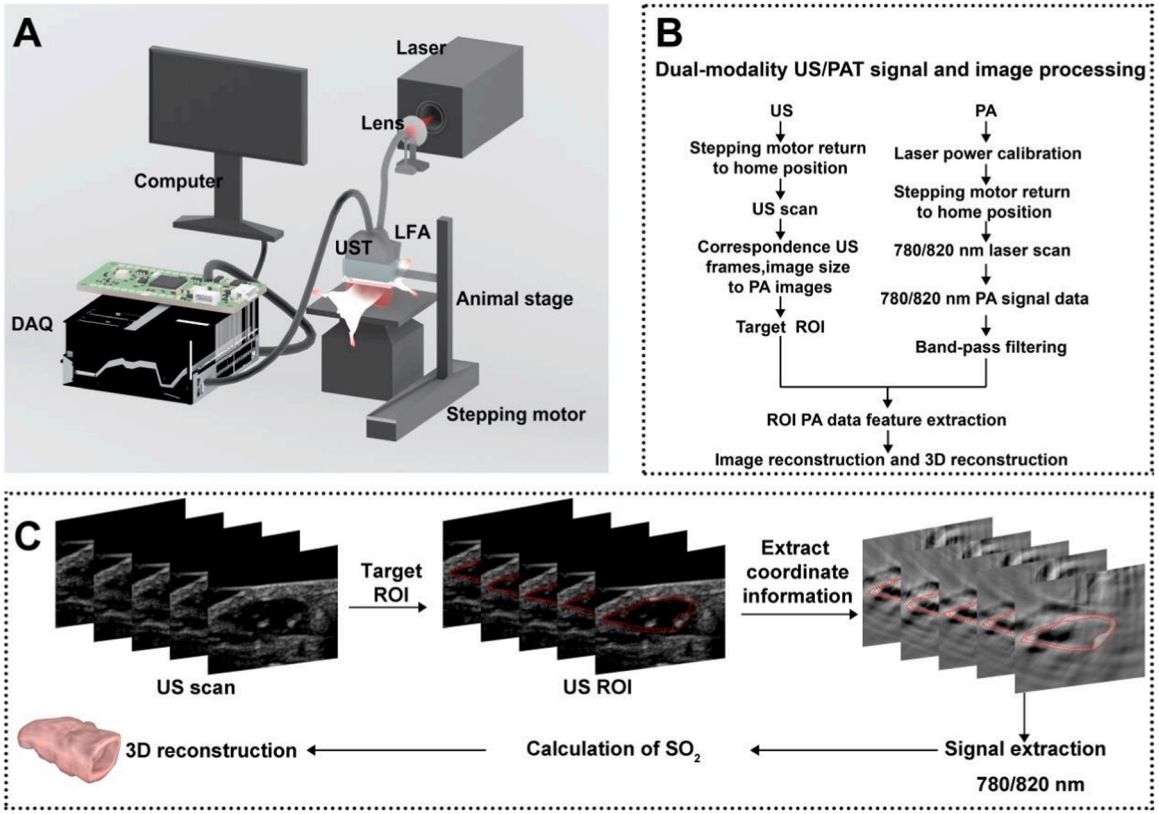

Fig. 4. Schematic diagram of the dual-modality US/PAT system and data processing. (A) Schematic of the dual-modality US/PAT imaging system. (B) Workflow of dual-modality US/PAT signal and image processing. (C) Process for 3D reconstruction. Note: UST, ultrasound transducer; LFA, linear fiber array; DAQ, Data Acquisition.

modality US/PAT transducer and the tissue.

Before scanning, the stepping motor was calibrated to the starting position, and respiratory movements of the thoracic cavity were monitored. Scans were initiated at the end of inhalation and continued until data for both wavelengths and ultrasonic measurements were collected, minimizing displacement from respiratory motion or other factors.

2.4. Image reconstruction and analysis

All data were reconstructed in real-time using the back-projection algorithm in LabVIEW (National Instruments, USA) and archived for further analysis in MATLAB R2023a (MathWorks, Inc., USA). To reduce noise, a band-pass filter (0.2–10 MHz) was applied during offline processing.

To account for optical fluence variations at 780 nm and 820 nm when calculating SO_2, a laser energy meter (Pulsar-1, Ophir, Jerusalem, Israel) was used to measure and calibrate optical intensity.

PA calculates SO_2 similarly to near-infrared spectroscopy, treating HB and HBO_2 as the primary absorbing compounds at each wavelength (λ_i). The blood absorption coefficient μ_a (in cm^{-1}) is expressed as [21]:

$$\mu_a(\lambda_i) = \varepsilon_{HB}(\lambda_i)[HB] + \varepsilon_{HBO_2}(\lambda_i)[HBO_2] \quad (1)$$

Where ε_{HB} and ε_{HBO_2} are known molar extinction coefficients (in cm^{-1} M^{-1}) of HB and HBO_2 at wavelength λ_i, and *[HB]* and *[HBO_2]* are the concentrations of the two types of hemoglobin, respectively. Since the amplitude of the acquired localized PA signal $\varphi(\lambda_i, x, y, z)$ is proportional to the local optical energy deposition, we can replace $\mu_a(\lambda_i)$ with $\varphi(\lambda_i, x, y, z)$. The variables x, y, and z represent the coordinates within three-dimensional space. Thus, utilizing dual wavelengths allows for the relative calculation of $[HB]_{(x, y, z)}$ and $[HBO_2]_{(x, y, z)}$. Therefore, the SO_2 can then be calculated using:

$$SO_{2(x,\ y,\ z)} = \frac{[HBO_2]_{(x,\ y,\ z)}}{[HBO_2]_{(x,\ y,\ z)} + [HB]_{(x,\ y,\ z)}} \quad (2)$$

According to Eqs. (1) and (2), while it is feasible to calculate SO_2.

The same ultrasound system and stepping motor were used for localizing and visualizing the target area, maintaining the same scan range and step frequency. As shown in Fig. 4B, the dimensions of the ultrasound imaging region were adjusted before PAT imaging to ensure proper alignment.

After acquiring both ultrasound and PAT images, the ultrasound frames were temporally synchronized with their corresponding PAT frames. As illustrated in Fig. 4C, regions of the intestinal wall within the subcutaneous space were identified in the ultrasound images, focusing on areas that clearly displayed the three-layer intestinal structure. This structure consisted of low, intermediate, and high echogenicity layers, arranged from innermost to outermost. Regions affected by gas artifacts were carefully excluded. The positional information of the delineated ROI was extracted and mapped onto the corresponding PA frames. PAT data from these regions were then used for subsequent 3D reconstruction.

2.5. Pathology and molecular assessment

Two experienced gastrointestinal surgeons independently assessed intestinal strangulation using empirical judgment and a gross scoring system (Table 1).

After imaging and gross specimen assessment, subcutaneous intestinal tissues were promptly excised, fixed in 4 % paraformaldehyde, embedded in paraffin, and sectioned for H&E staining. Pathological alterations were observed and evaluated under an optical microscope. Two researchers independently assessed tissue damage using Chiu's grading system under blinded conditions, with criteria outlined in Table 2 [22]. In case of disagreement, a third pathologist was consulted to determine the final result.

Table 1
Surgeons' empirical judgment and gross specimen evaluation.

Surgeons' empirical judgment	Gross specimen evaluation	
Normal intestine	0 score	No congestion or hemorrhage in the intestinal wall, with normal mucosa
	1 score	Congestion and hemorrhage in the intestinal wall, with normal mucosa
Indeterminate intestine	2 score	Congestion and hemorrhage in the intestinal wall, with mucosal ulceration covering less than 10 % of the area
	3 score	Congestion and hemorrhage in the intestinal wall, with mucosal ulceration covering 10–25 % of the area
Necrotic intestine	4 score	Congestion and hemorrhage in the intestinal wall, with mucosal ulceration covering 25–50 % of the area
	5 score	Congestion and hemorrhage in the intestinal wall, with mucosal ulceration covering more than 50 % of the area

Table 2
Chiu's grading system of intestinal mucosal injury.

Point	Description
0	The presence of normal small intestinal villi
1	The widening of inter-villous spaces concomitant with capillary congestion at the villi tips
2	The expansion of inter-villous spaces with moderate separation between the epithelial and lamina propria layers
3	Extensive separation between the epithelial and lamina propria layers on both sides of the small intestinal villi
4	Villous damage, accompanied by exposed capillaries within the lamina propria and an increased influx of inflammatory cells
5	Lamina propria destruction, hemorrhage

2.6. Immunohistochemical staining

Immunohistochemical (IHC) staining was performed to assess the hypoxic condition, barrier integrity, and inflammatory status of intestinal samples. Antibodies used included HIF-1α (1:100, bs-20399R, Bioss, USA), ZO-1 (1:2000, 21773–1-AP, Proteintech, China), Occludin (1:8000, 27260–1-AP, Proteintech, China), and TNF-α (1:400, 60291–1-Ig, Proteintech, China).

The standardized IHC protocol involved deparaffinizing, rehydrating, and performing antigen retrieval in citrate buffer. Sections were permeabilized with 0.3 % Triton X-100 in TBS for 15 minutes, then blocked with 10 % goat serum in BSA for 2 hours at room temperature. After overnight incubation at 4 °C with primary antibodies, endogenous peroxidase was blocked using 0.3 % hydrogen peroxide for 15 minutes. Slides were treated with a horseradish peroxidase-conjugated secondary antibody (1:200, G1213, Servicebio, China) for 1 hour at room temperature, followed by washes in 0.025 % Triton X-100 in TBS. Visualization was performed with the DAB Substrate Kit (G1212, Servicebio) for 3 minutes, and hematoxylin counterstaining was applied for 5 minutes. Staining results were analyzed using the IHC Profiler plugin in ImageJ/Fiji (version 2.0.0, NIH) [23]. The plugin uses color deconvolution to distinguish cytoplasmic and nuclear staining, calculates grayscale values, and determines the percentage of staining intensity with corresponding scores.

2.7. Blood molecular markers: enzyme-linked immunosorbent assays

Several blood molecular markers were evaluated to assess intestinal oxidative stress, antioxidant capacity, and tissue damage. Malondialdehyde (MDA), a marker of oxidative stress, was quantified using an MDA assay kit (BC0025, Solarbio, China). Superoxide dismutase (SOD), an indicator of antioxidant capacity, was measured with a SOD assay kit

(BC5165, Solarbio, China). Diamine oxidase (DAO), linked to intestinal barrier integrity, was assessed using a DAO assay kit (BC1285, Solarbio, China). L-lactic acid (L-LA), associated with intestinal hypoxia, was analyzed with an L-LA assay kit (BC2235, Solarbio, China). All assays followed the manufacturer's protocols, and all aforementioned blood molecular markers quantified with a microplate reader.

2.8. Statistical analysis

The data utilized for dual-modality US/PAT imaging are derived from entire segmental scanning of the intestinal section (Fig. 2). US/PAT parameters, including mean, median, range (100 %, 80 %, 60 %), kurtosis, and skewness, were used as statistical measures to describe the shape of data distributions, with definitions and calculation methods detailed in Table 3. Differences in CEUS, US/PAT, pathological features, and molecular markers among the Control, Sim-IO, and Str-IO groups were analyzed using one-way analysis of variance (ANOVA), with post-hoc pairwise comparisons conducted using Turkey's multiple comparisons test. The diagnostic performance of CEUS, PAT, pathological features, and molecular markers in distinguishing between the Control, Sim-IO, and Str-IO groups was evaluated using ROC curve analysis. Optimal cutoff values were determined using the Youden index. All statistical analyses were conducted with GraphPad Prism 8 (GraphPad Software Inc., USA) and MATLAB 2023a (The MathWorks, Inc., USA). A P-value < 0.05 was considered statistically significant.

Table 3
Distribution characteristics and calculation formulas of SO_2 in dual-modality ultrasound/photoacoustic tomography imaging.

Distribution characteristics	Definitions	Formulas
Mean	The mean is the average of a set of numbers, calculated by summing all the values and dividing by the total number of values. The formula is: $Mean = \frac{\sum_{i=1}^{n} x_i}{n}$	(3)
Median	The median is the middle value in a sorted list of numbers. If the list has an odd number of values, it is the central one. If it has an even number, it is the average of the two central values. The formula is, If n is odd: $Median = x_{(\frac{n+1}{2})}$ If n is even: $Median = \frac{x_{(\frac{n}{2})} + x_{(\frac{n}{2}+1)}}{2}$	(4.1) (4.2)
Range (100 %, 80 %, 60 %)	The range (100 %, 80 %, 60 %) refers to specific percentiles used to describe the spread or dispersion of a dataset. Specifically speaking: 100 % range: This represents the full extent of the data, from the minimum to the maximum value. 80 % range: This represents the range within which 80 % of the data points fall, often calculated by excluding the lowest 10 % and the highest 10 %. 60 % range: This represents the range within which 60 % of the data points are concentrated, typically calculated by excluding the lowest 20 % and the highest 20 %.	\
Kurtosis	Kurtosis measures the "tailedness" of the distribution. High kurtosis indicates a distribution with heavy tails and a sharp peak, while low kurtosis suggests lighter tails and a flatter peak. The formula is: $Kurtosis = \frac{n(n+1)}{(n-1)(n-2(n-3))}\sum(\frac{x_i-\overline{x}}{s})^4 - \frac{3(n-1)^2}{(n-2)(n-3)}$	(5)
Skewness	Skewness measures the asymmetry of the distribution. Positive skewness indicates a distribution with a longer right tail, while negative skewness indicates a longer left tail. The formula is: $Skewness = \frac{n}{(n-1)(n-2)}\sum(\frac{x_i-\overline{x}}{s})^3$	(6)

Note: where n is the number of observations, x_i are the represents each value, $\overline{x}$ is the mean, and s is the standard deviation.

3. Results

3.1. Analysis of CEUS curves and characteristics for diagnosis of strangulation

In CEUS mode, a 2-minute imaging session was performed for the subcutaneous intestinal tract of each rat. As shown in Fig. 5A, contrast intensity-time parameters were extracted from three ROIs (about 2 mm^2 each). Fig. 5A also shows CEUS examples and corresponding time-intensity curves for the Control, Sim-IO, and Str-IO groups, with ROI borders matching the curve colors. Time-intensity curve features included PKI, AUC, TTP, HDT, MTT, RT, and AS, which detailed significance can be referenced in the preceding section "Methods 2.2 CEUS examination".

The results showed significant differences in PKI among the Control, Sim-IO, and Str-IO groups (Fig. 5B), with values of 12.60 ± 2.02, 10.15 ± 2.10, and 4.25 ± 2.09 dB, respectively. Pairwise comparisons showed statistical significance, with $P < 0.05$ between Control and Sim-IO, and $P < 0.001$ between Control and Str-IO and between Sim-IO and Str-IO.

AUC also distinguished between Sim-IO and Str-IO (Fig. 5C), with values of 622.03 ± 215.39 and 337.36 ± 526.47 ($P < 0.001$). However, there was no statistical difference in AUC between Control (788.43 ± 223.27) and Sim-IO (622.03 ± 215.39) with a P-value of 0.08.

Among other parameters, TTP exhibited statistical differences between Control and Str-IO (Fig. 5D), with values of 12.32 ± 3.59 and 19.80 ± 9.17 s, respectively, ($P < 0.05$). The TTP in the Sim-IO group was recorded at 14.51 ± 3.66 s, with no significant differences compared to the other groups.

RT for Control, Sim-IO and Str-IO was 6.43 ± 2.50, 8.17 ± 2.54, and 8.35 ± 5.50 s (Fig. 5E), displaying no statistical significance (all $P > 0.05$).

MTT for Control, Sim-IO and Str-IO was 27.05 ± 6.58, 26.39 ± 5.78, and 24.28 ± 9.87 s, respectively (Fig. 5F), showing no statistical significance (all $P > 0.05$).

The HDT for Control, Sim-IO and Str-IO was 42.87 ± 12.38, 41.22 ± 9.70 and 30.97 ± 15.53 s, respectively (Fig. 5G). Though Str-IO's HDT was lower than Control and Sim-IO, there was no statistical difference (all $P > 0.05$).

Finally, AS for Control, Sim-IO, and Str-IO was 1.56 ± 0.65, 1.08 ± 0.37, and 0.76 ± 0.78 (Fig. 5H), with no statistical significance found (all $P > 0.05$).

The Chiu's score was utilized as the gold standard, with a score of 4 or higher indicative of irreversible ischemia and strangulation. Details regarding the Chiu's score are provided in Method 2.5. The ROC curves for CEUS parameters in the diagnosis of strangulation are illustrated in Fig. 3I and J.

Among the indicators with high diagnostic AUROC, the PKI achieved an AUROC of 0.995 (95 % CI 0.981–1.000). A cut-off value of ≤ 8.265 dB yielded the highest Youden index, resulting in a sensitivity of 96.2 % and a specificity of 100 %. The AUC was 0.979 (95 % CI 0.941–1.000), with a cut-off of ≤ 397.18, also yielding the highest Youden index, identifying strangulation with a sensitivity of 96.2 % and a specificity of 93.3 %. The AS demonstrated an AUROC of 0.779 (95 % CI 0.604–0.955), with the optimal cut-off ≤ 0.91 s, providing a sensitivity of 76.9 % and a specificity of 80 %.

Other CEUS parameters, including TTP, RT, MTT, and HDT, exhibited AUROCs of 0.595 (95 % CI 0.380–0.810), 0.431 (95 % CI 0.179–0.683), 0.426 (95 % CI 0.201–0.651), and 0.330 (95 % CI 0.132–0.529), respectively, as shown in Fig. 5J.

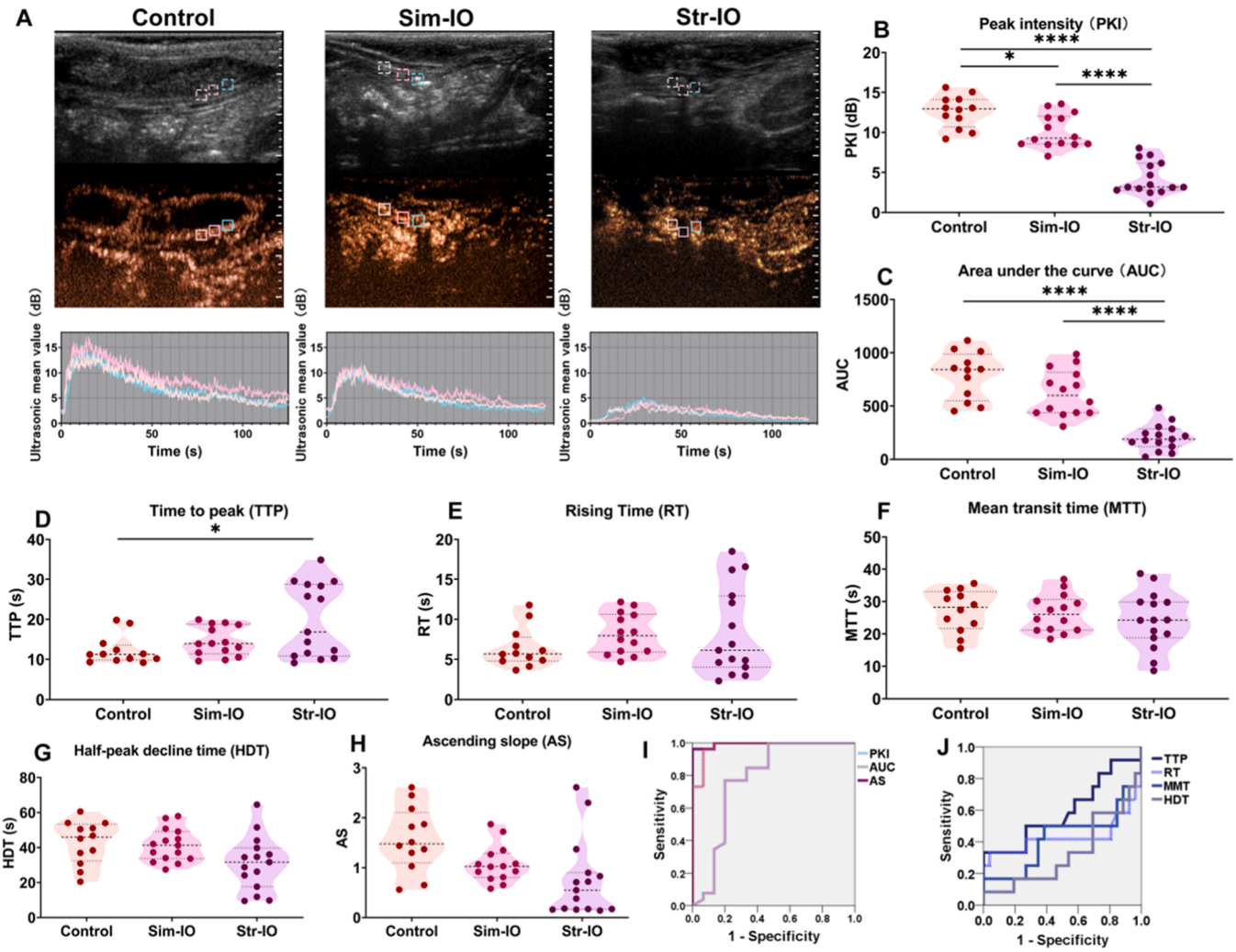

Fig. 5. CEUS images and feature parameters for diagnosing strangulation. (A) CEUS images and corresponding time-intensity curves, with the ROI border colors matching the colors of the time-intensity curves below. The dashed lines on the right side of the ultrasound and CEUS images represent the scale, with 1 cm between long lines and 2 mm between short lines. CEUS feature parameters for the Control, Sim-IO, and Str-IO groups: (B) peak intensity (PKI), (C) area under the curve (AUC), (D) time to peak (TTP), (E) rising time (RT), (F) mean transit time (MTT), (G) half-peak decline time (HDT), (H) ascending slope (AS). ROC curves of CEUS feature parameters for diagnosing strangulation, using (I) PKI, AUC, and AS, (J) TTP, RT, MTT, and HDT. Data presented as mean ± SD. Each group consisted of five rats, with each rat assessed in triplicate, yielding a total of 15 data points. One rat in the Control group died during anesthesia, likely due to health issues or stress-related complications, reducing the data point to 12. Comparison among the three groups was conducted using ordinary one-way ANOVA, with post-hoc pairwise comparisons performed using Tukey's multiple comparisons test. *$P < 0.05$, * ** *$P < 0.0001$.

3.2. Diagnosis performance of dual-modality US/PAT and features for intestinal strangulation

Using data obtained from US/PAT dual-modality imaging, three-dimensional visualization was performed. As depicted in Fig. 6A, the Control group exhibited higher SO_2 values, indicated by greater red saturation, followed by the Sim-IO group, while the Str-IO group displayed the lowest red saturation. Subsequently, the average SO_2 values are presented in Fig. 6B. The mean SO_2 was 51.51 ± 11.57 % in the Control group, 48.52 ± 3.91 % in the Sim-IO group, and 46.00 ± 3.04 % in the Str-IO group. Although a trend toward decreasing SO_2 levels in conjunction with increased strangulation severity was observed, the differences among the three groups were not statistically significant ($P = 0.728$).

While the lack of statistically significant differences in SO_2 among the three groups may be discouraging, it raises the question of whether dual-modality US/PAT technology is capable of differentiating between intestines that are strangulated. To further elucidate this issue, we extracted all SO_2 data and used frequency distribution histograms, which revealed distinct patterns in the SO_2 distributions across the groups, as shown in Fig. 6C. The SO_2 distribution in the Control group exhibited a tendency towards a normal distribution, whereas the Sim-IO group demonstrated a distribution characterized by a sharper peak, indicating a higher concentration of values. This trend was even more pronounced in the Str-IO group, where the peak became increasingly defined. The kurtosis for each group was calculated (Fig. 6D), yielding mean values of 3.76 ± 0.79 for the Control group, 21.72 ± 9.15 for the Sim-IO group, and 141.20 ± 138.07 for the Str-IO group. The observed differences were found to be statistically significant, with *P*-values of 0.0066 for the comparison between the Control and Str-IO groups, and 0.0183 for the comparison between the Sim-IO and Str-IO groups; however, no significant difference was detected between the Control and Sim-IO groups ($P = 0.8951$). Two samples from the Str-IO group showed significantly elevated kurtosis, exceeding the mean plus two standard deviations, and were thus identified as outliers and removed from the analysis.

The skewness of the SO_2 distribution for each group was calculated and is illustrated in Fig. 6E. The Control group exhibited a mean

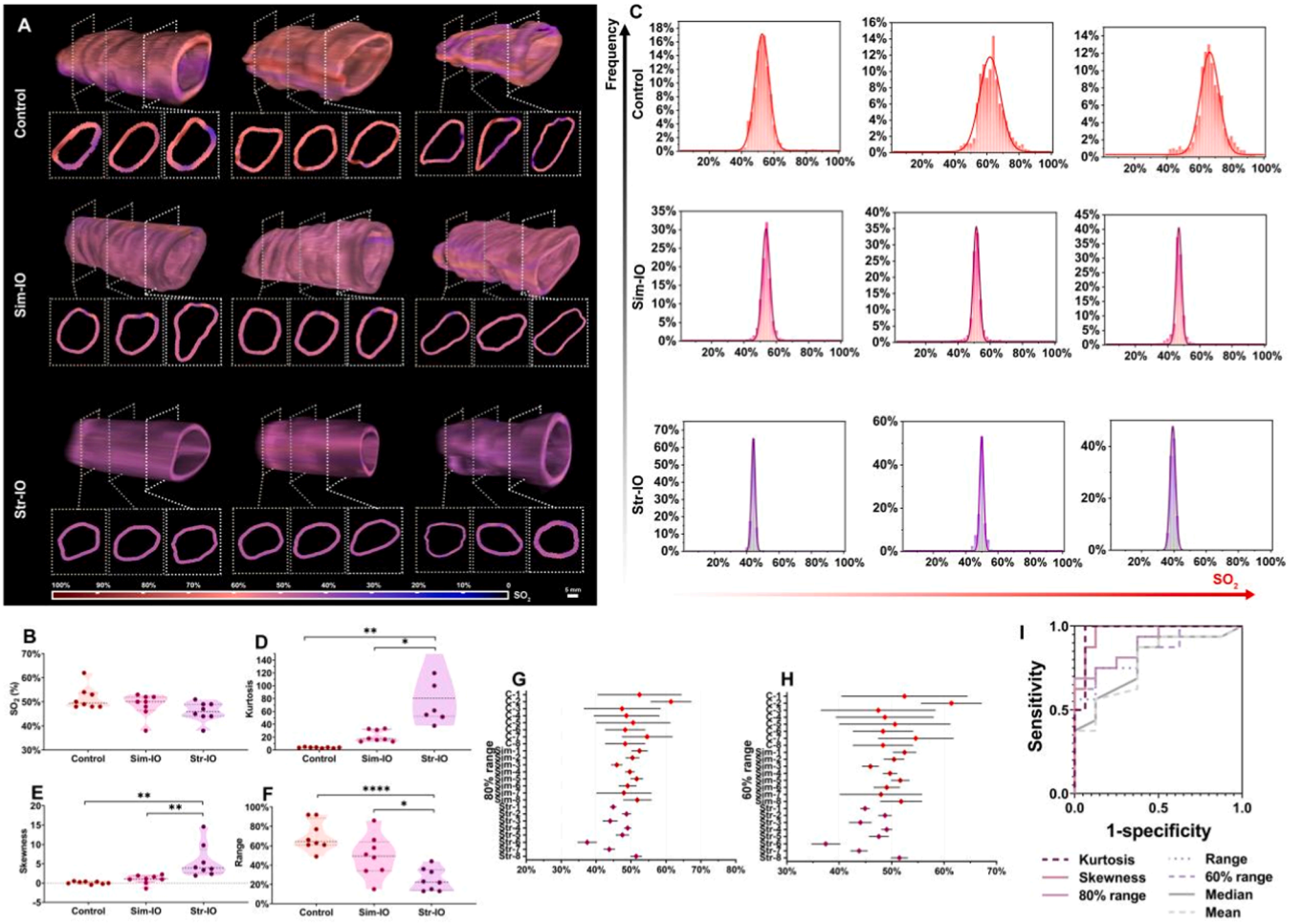

Fig. 6. Dual-modality US/PAT images, distribution characteristics and diagnostic performance. (A) Three-dimensional dual-modality US/PAT images for the Control, Sim-IO, and Str-IO groups, each additionally presenting three cross-sectional views of the reconstructed segment. Each row represents three randomly selected samples. The white short bar represents a 5-mm scale marker. (B) SO_2 of the Control, Sim-IO, and Str-IO groups. (C) Examples of the frequency distribution histograms of SO_2 for the Control, Sim-IO, and Str-IO groups. (D) Kurtosis, (E) skewness and (F) range of SO_2 distribution. (G) 80 % distribution range of SO_2. (H) 60 % distribution range of SO_2. (I) ROC curves of SO_2 mean, median, skewness, kurtosis, range, 80 % range and 60 % range. The statistical analysis utilized the entire dataset, rather than being confined to the exhibited samples. The data present the mean ± SD ($n = 8$). Comparison among the three groups was performed using one-way ANOVA, with post-hoc pairwise comparisons conducted using Turkey's multiple comparisons test. *$P < 0.05$, * *$P < 0.01$, * ** *$P < 0.0001$. Note: In Fig. 6D, two Str-IO samples with kurtosis exceeding the mean plus two standard deviations were identified as outliers and removed from the analysis.

skewness of 0.09 ± 0.33, indicating a distribution that is approximately symmetrical. In contrast, the Sim-IO group demonstrated a mean skewness of 0.93 ± 1.16, suggesting a slight positive skew with data concentrated on the left side of the distribution. The Str-IO group showed a more pronounced positive skew, with a mean skewness of 5.64 ± 4.36, indicating that a larger proportion of data fell on the left side compared to the previous two groups.

Additionally, the range of SO_2 values for each group was computed, as shown in Fig. 6F. The ranges for the Control, Sim-IO, and Str-IO groups were found to be 70.24 ± 15.71 %, 45.27 ± 20.95 %, and 28.63 ± 15.49 %, respectively, reflecting a gradual decline. These differences were statistically significant, with a *P*-value of < 0.0001 between the Control and Str-IO groups, and a *P*-value of 0.0233 between the Sim-IO and Str-IO groups; however, no statistically significant difference was observed between the Control and Sim-IO groups ($P = 0.0527$).

To account for potential outliers generated during the imaging and calculations, the distributions corresponding to the largest 80 % and 60 % of SO_2 were extracted, as illustrated in Fig. 6G (80 % range) and 6 H (60 % range). It was observed that the distribution of the Control group (C1 ~ C8) was significantly wider than those of the Sim-IO (Sim-1 ~ Sim-8) and Str-IO groups (Str-1 ~ Str-8). An attempt was made to summarize whether differences existed in the distribution ranges among the three groups; however, no significant differences were detected.

A pathological Chiu's score of 4 or higher is indicative of irreversible strangulation. ROC curves were employed to evaluate the diagnostic performance of SO_2 mean, median, kurtosis, skewness, range, 80 % range, and 60 % range in identifying intestinal strangulation (Fig. 6I), with AUROCs of 0.777 (95 % CI 0.581–0.973), 0.789 (95 % CI 0.600–0.978), 0.969 (95 % CI 0.902–1.000), 0.969 (95 % CI 0.908–1.000), 0.867 (95 % CI 0.721–1.000), 0.898 (95 % CI 0.775–0.891) and 0.867 (95 % CI 0.721–1.000). The results indicated that kurtosis and skewness serve as effective indicators for distinguishing the presence of strangulation. When kurtosis was set at ≥ 35.61, the Youden index reached its maximum value, yielding a sensitivity of 100 % and a specificity of 93.7 %. Similarly, at a skewness value of ≥ 1.92, the maximum Youden index was achieved, resulting in a sensitivity of 100 % and a specificity of 87.5 %.

3.3. Experiment-based judgement, gross scoring of surgeons and Chiu's score for diagnosing strangulation

After surgery and imaging assessment, the rat's skin sutures was incised (Fig. 7A). Two experienced gastrointestinal surgeons, each with

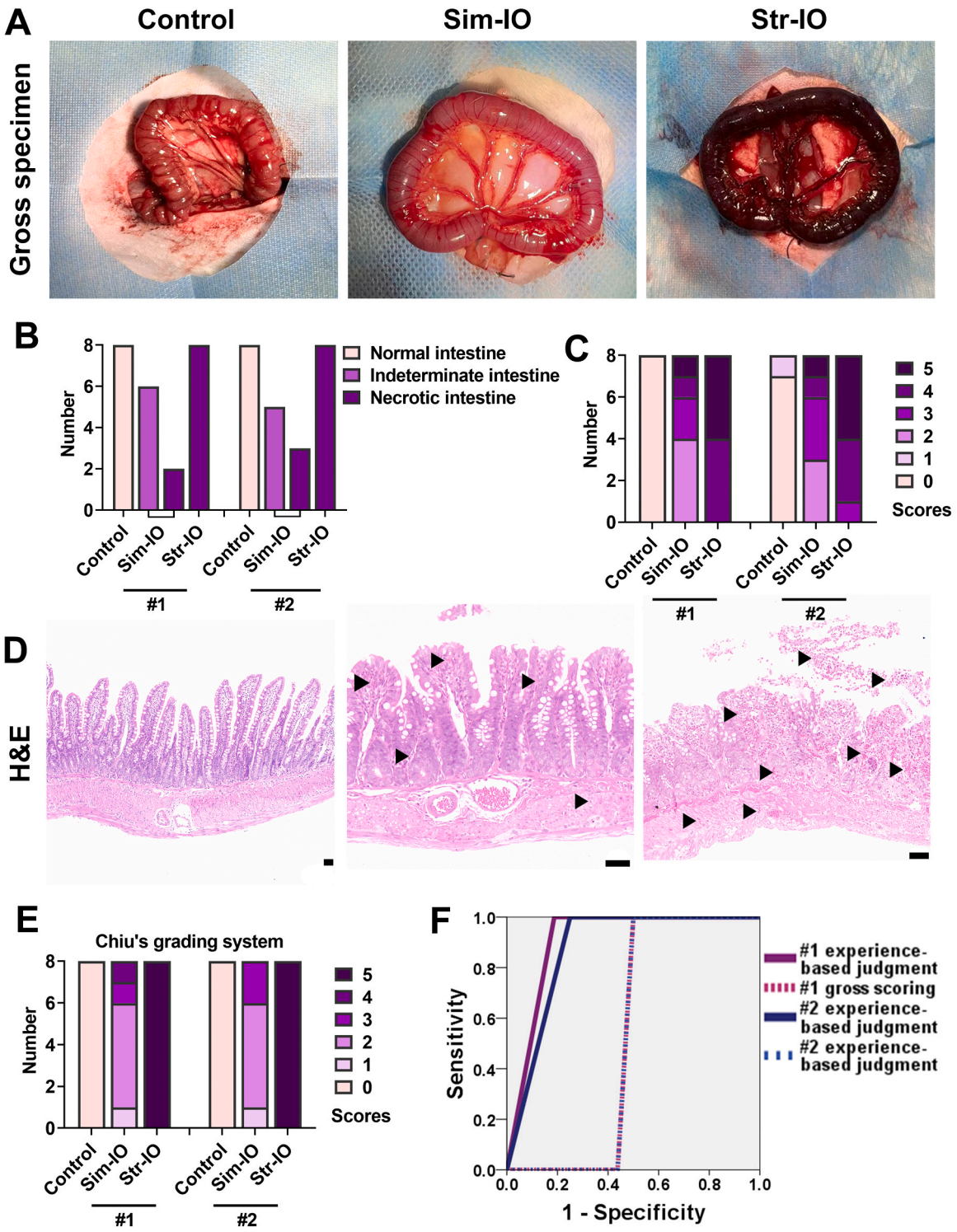

Fig. 7. IO gross specimen and Chiu's score analysis. (A) Gross specimen of Control, Sim-IO and Str-IO examples. (B) Surgeons experience-based judgment of the condition of strangulation of Control, Sim-IO and Str-IO. (C) Gross scoring by Surgeons. For detailed scoring criteria, please refer to Method 2.5. (D) Examples of H&E staining of Control, Sim-IO and Str-IO. The area indicated by the triangle was identified as the region of hemorrhage. (E) Chiu' grading system of Control, Sim-IO and Str-IO. Please refer to Method 2.5. (F) ROC curves of Surgeons experience-based judgment and gross scoring. The black bar representing the length of 50 μm.

more than 10 years of experience, subjectively evaluated the status of the subcutaneous intestinal tract. The animal groupings were masked to ensure that the surgeons made their assessments independently. In the Control group, both surgeons achieved a 100 % accuracy rate in their evaluations. In cases of Sim-IO, surgeon 1 classified 75 % (6/8) as indeterminate intestine and 25 % (2/8) as necrotic intestine. In contrast, Surgeon 2 assessed 62.5 % (5/8) as indeterminate intestine and 37.5 % (3/8) as necrotic intestine. In the Str-IO group, both surgeons also achieved a 100 % accuracy rate in their assessments (Fig. 7B).

In the context of gross scoring, it is generally accepted that when the score reaches 4 or 5, the intestinal damage may be considered irreversible or indicative of a poor prognosis. This is due to the fact that at a score of 4, the extent of the wall damage involves 25–50 % of the surface area, while at a score of 5, it exceeds 50 %. In the Control group, Surgeon

1 assigned eight scores of 0, while Surgeon 2 recorded 7 scores of 0 and one score of 1. In the Sim-IO group, Surgeon 1 assigned four scores of 2, two scores of 3, one score of 4, and one score of 5; Surgeon 2 assigned three scores of 2, three scores of 3, one score of 4, and one score of 5. In the Str-IO group, Surgeon 1 assigned four scores of 4 and four scores of 5; Surgeon 2 assigned one score of 3, three scores of 4, and four scores of 5 (Fig. 7C).

The judgment made by the surgeons based on their experience is not necessarily correct. Therefore, a comprehensive pathological assessment was conducted, initially employing H&E staining (Fig. 7D) to evaluate the extent of intestinal injury using Chiu's grading system, with the results presented in Fig. 7E. In general, both pathologists reached complete concordance on Chiu's grades for all Control and Str-IO groups. In the Sim-IO group, they both assigned one score of 1 and five scores of 2. However, for the remaining two samples, Pathologist 1 assigned one score of 3 and one score of 4, while Pathologist 2 assessed both samples as scoring 3. Therefore, a third pathologist was involved, and consensus was ultimately reached, adopting the grades provided by Pathologist 2.

The ROC curves for the assessment of the surgeons' evaluations based on experience and gross specimen scoring were analyzed according to Chiu's scoring system, as shown in Fig. 7F. The AUROC for experience-based judgments by Surgeon 1 and Surgeon 2 were 0.906 (95 % CI 0.783–1.000) and 0.875 (95 % CI 0.734–1.000), respectively. In contrast, the AUROC for evaluations based on gross scoring was 0.531 (95 % CI 0.291–0.772), indicating that this approach does not seem to reach the performance levels achieved through purely experiential judgment.

3.4. Expression of HIF-1α and its correlation with strangulation

HIF-1α expression was observed in all Control, Sim-IO, and Str-IO groups. As depicted in Fig. 8A, which also shows an enlarged section of an individual villus, the expression of HIF-1α increased progressively with the severity of hypoxia and ischemia, manifesting as elevated expression in both the cytoplasm and nucleus. An image analysis system was utilized to quantify the percentages of positive and low-positive expression in the nucleus and cytoplasm, as illustrated in Fig. 8B-E.

Specifically, the positive cytoplasmic expression percentages (Fig. 8B) for the Control, Sim-IO, and Str-IO groups were 0.76 ± 0.37 %, 1.76 ± 0.80 %, and 3.08 ± 1.22 %, respectively, with statistically significant differences. The *P*-value for the difference between the Control and Str-IO groups was < 0.0001, while the *P*-value for the difference between the Sim-IO and Str-IO groups was 0.0164. No statistically significant difference was noted between the control and Sim-IO groups, with a *P*-value of 0.0783. In the nucleus, the positive percentage of expression is illustrated in Fig. 8C, where the Control, Sim-IO, and Str-IO groups were 0.26 ± 0.16 %, 1.55 ± 1.12 %, and 3.43 ± 1.69 %, respectively, with statistically significant differences noted. The *P*-value for the comparison between the Control and Str-IO groups was

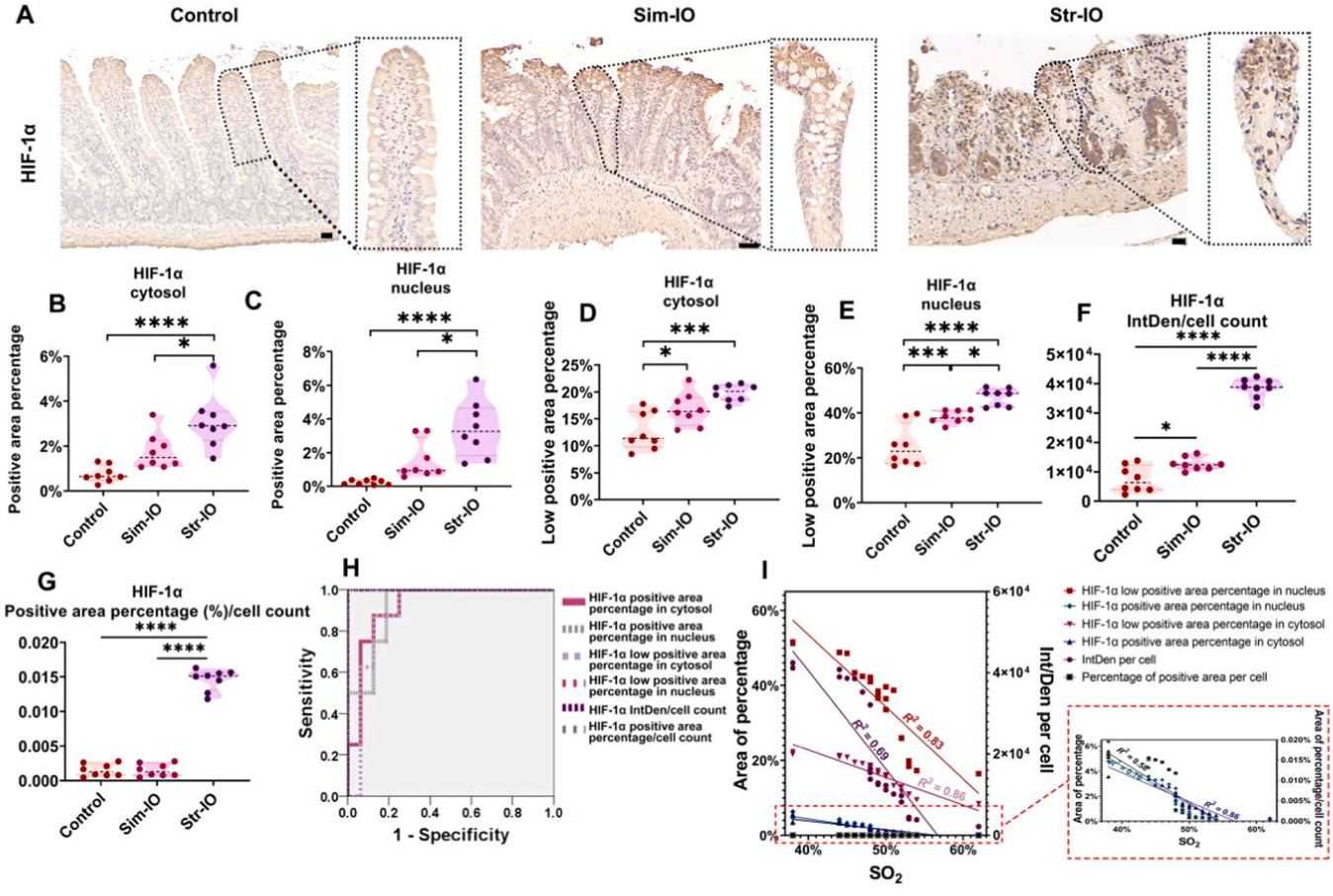

Fig. 8. Expression of HIF-1α by IHC staining and its correlation with strangulation. (A) HIF-1α staining and expression in Control, Sim-IO and Str-IO group. The magnified image of an individual villus is depicted in the dashed portion. (B) HIF-1α positive area percentage in cytosol, (C) HIF-1α positive area percentage in nucleus, (D) HIF-1α low positive area percentage in cytosol, (E) HIF-1α low positive area percentage in nucleus, (F) integrated density (IntDen) per cell of HIF-1α, (G) percentage of positive area per cell of HIF-1α of Control, Sim-IO and Str-IO group. (H) ROC curves of HIF-1α related parameters for diagnosing strangulation. (I) Relationship between HIF-1α expression and SO_2. The date present the mean ± SD ($n = 8$ per group). Comparison among the three groups was performed using one-way ANOVA, with post-hoc pairwise comparisons conducted using Turkey's multiple comparisons test. The black bar representing the length of 50 μm. *$P < 0.05$, * **$P < 0.001$, * ** *$P < 0.0001$.

< 0.0001, while the *P*-value for the comparison between the Sim-IO and Str-IO groups was 0.0113. However, no statistically significant difference was observed between the Sim-IO and Control groups, with a *P*-value of 0.0926.

The positive expression of HIF-1α was not high among all groups, leading to a subsequent analysis of the percentage of low positive expression. As shown in Fig. 8D, the percentages of low positive expression in the cytosol for the Control, Sim-IO, and Str-IO groups were 12.73 ± 3.50 %, 16.76 ± 3.10 %, and 19.81 ± 1.57 %, respectively, with statistically significant differences observed. The *P*-value for the comparison between the Control and Sim-IO groups was 0.0259, and the *P*-value for the comparison between the Control and Str-IO groups was 0.0002. No statistically significant difference was found between the Sim-IO and Str-IO groups, with a *P*-value of 0.1042. As depicted in Fig. 8E, the expression percentage of low positive HIF-1α in the nucleus was 25.27 ± 9.31 % for the Control group, 38.21 ± 2.82 % for the Sim-IO group, and 47.14 ± 3.90 % for the Str-IO group, with statistically significant differences observed. The *P*-value for the comparison between the Control and Sim-IO groups was 0.0009, while the *P*-value for the Control versus Str-IO comparison was less than 0.0001. A statistically significant difference was also noted between the Sim-IO and Str-IO groups ($P = 0.02$).

Simultaneously, it was observed that the expression of HIF-1α within the Str-IO group was heterogeneous (Fig. 8A), potentially attributable to the presence of tissue strangulation and cellular structural damage. Consequently, the integrated density (IntDen) per cell and the percentage of positive area (%) per cell were quantified. Results indicated that as the severity of ischemia increased in the Control, Sim-IO, and Str-IO groups, both the IntDen of HIF-1α expression per cell and the positive area percentage (%) per cell increased (as illustrated in Fig. 8F and G, respectively). Statistical analysis revealed significant differences in HIF-1α expression (IntDen per cell, Fig. 8F) among the Control, Sim-IO, and Str-IO groups, with a *P*-value of 0.048 between control and Sim-IO. Moreover, significant differences were noted between control and Sim-IO, as well as between Control and Str-IO, with $P < 0.001$ for both comparisons. Regarding the positive area percentage per cell (Fig. 8G), a statistically significant difference was identified between the Control and Str-IO groups ($P < 0.0001$). Additionally, a statistically significant difference was noted between the Sim-IO and Str-IO groups ($P < 0.0001$); however, no significant difference was found between the Control and Sim-IO groups ($P > 0.05$).

Fig. 8H presents the ROC curves for the following parameters and their AUROC values: positive area of HIF-1α in the cytosol (0.922, 95 % CI 0.812–1.000); positive area of HIF-1α in the nucleus (0.922, 95 % CI 0.816–1.000); low positive area of HIF-1α in the cytosol (0.898, 95 % CI 0.765–1.000); low positive area of HIF-1α in the nucleus (1.000, 95 % CI 1.000–1.000); IntDen per cell of HIF-1α (1.000, 95 % CI 1.000–1.000); positive area percentage per cell of HIF-1α (1.000, 95 % CI 1.000–1.000). The Youden index was maximized when the cut-off value for the HIF-1α positive area in the cytosol was set at ≥ 2.06 %, resulting in a sensitivity and specificity of both 87.5 %. For the HIF-1α positive area in the nucleus, a cut-off value of ≥ 1.16 % achieved a sensitivity of 100 % and a specificity of 81.2 %. Similarly, a cut-off of ≥ 16.93 % for the HIF-1α low positive area in the cytosol yielded a sensitivity of 100 % and a specificity of 75 %. The highest AUROC was observed for the HIF-1α low positive area in the nucleus, with a cut-off of ≥ 41.75 %, reaching a sensitivity and specificity of 100 %.

Due to the lack of a universally accepted and precise metric for assessing tissue SO_2, HIF-1 serves as a reliable biomarker for evaluating the degree of tissue hypoxia. HIF-1 is a heterodimeric protein consisting of a constitutively expressed beta subunit and an alpha subunit regulated by tissue oxygen tension [24]. Notably, the expression of the alpha subunit, HIF-1α, is negatively correlated with tissue oxygen saturation [25]. Therefore, in this study, IHC expression of HIF-1α was employed as the standard for assessing tissue hypoxia. We aimed to evaluate the accuracy of US/PAT in diagnosing hypoxia by comparing its diagnostic accuracy with that of HIF-1α expression. A linear regression analysis was conducted between the parameters evaluating HIF-1α expression and the SO_2. The results shown in Fig. 8I reveal a negative correlation between SO_2 and HIF-1α expression. Notably, SO_2 exhibited a strong negative correlation with the percentage of low positive area of HIF-1α in the nucleus ($R^2 = 0.83$), the low positive area of HIF-1α in the cytosol ($R^2 = 0.86$), and the percentage of positive area of HIF-1α in the nucleus ($R^2 = 0.86$), with R^2 values exceeding 0.8. These results indirectly affirm the accuracy of SO_2 measurements obtained through US/PAT.

3.5. Strangulation's relationship between inflammation and intestinal barrier function

The expression of TNF-α, indicative of the inflammatory status of the intestine, along with ZO-1 and Occludin, markers of barrier function, are illustrated in Fig. 9A. First, the expression of TNF-α in the cytoplasm and nucleus across the groups was assessed in terms of the percentage of positive and low-positive staining. As shown in Fig. 9B, the mean percentage of the positive area for TNF-α in the cytosol was 2.25 ± 2.01 % in the Control group, 0.85 ± 0.24 % in the Sim-IO group, and 2.50 ± 1.47 % in the Str-IO group, with no significant differences (all $P > 0.05$). Fig. 9C shows that the mean percentage of the positive area for TNF-α in the nucleus was 1.31 ± 0.71 % for the Control group, 3.90 ± 1.29 % for the Sim-IO group, and 3.26 ± 1.25 % for the Str-IO group, with the highest value in the Sim-IO group. Significant differences were observed between the Control and Sim-IO groups ($P = 0.0004$) and between the Control and Str-IO groups ($P = 0.0059$). No significant difference existed between the Sim-IO and Str-IO groups ($P = 0.4927$). Fig. 9D illustrates the low percentage of TNF-α-positive area in the cytosol, with mean values of 17.95 ± 4.19 % for the Control group, 17.89 ± 1.50 % for the Sim-IO group, and 22.51 ± 2.85 % for the Str-IO group. Statistically significant differences were observed between the Control and Str-IO groups ($P = 0.0182$) and between the Sim-IO and Str-IO groups ($P = 0.0167$). Fig. 9E displays the low-positive area percentage of TNF-α in the nucleus, with mean values of 34.05 ± 7.37 % for the Control group, 55.74 ± 6.16 % for the Sim-IO group, and 43.21 ± 4.64 % for the Str-IO group. Statistically significant differences were found between the Control and Sim-IO groups ($P < 0.0001$), the Control and Str-IO groups ($P = 0.0190$), and the Sim-IO and Str-IO groups ($P = 0.0016$).

The assessment of barrier function through ZO-1 and Occludin is illustrated in the second and third rows of Fig. 3H. In the Control group, ZO-1 and Occludin are regularly expressed proteins within the intestinal villi. Under Sim-IO conditions, their expression remains largely unchanged; however, a notable uneven distribution is observed, which becomes more pronounced in the Str-IO group. These findings suggest that the barrier integrity of the intestinal villi is compromised in Sim-IO, while the disruption of the intestinal barrier is significantly exacerbated in Str-IO.

In the assessment of TNF-α expression, a rising trend was observed in the cytosolic expression among the Control, Sim-IO, and Str-IO groups, as illustrated in Fig. 9B and D. The ROC curve depicted in Fig. 7F shows that the AUROC for both positive and low-positive TNF-α expression in the cytosol was 0.805 (95 % CI 0.623–0.986) and 0.898 (95 % CI 0.774–1.000), respectively, in diagnosing strangulation. When the Youden index was maximized, a positive area percentage in the cytosol of ≥ 1.39 % yielded a sensitivity of 100 % and a specificity of 75 %. Furthermore, a low-positive area percentage in the cytosol of ≥ 18.47 % achieved a sensitivity of 100 % and a specificity of 68.7 %.

Fig. 9C and E indicate that the Sim-IO group demonstrated the highest expression of TNF-α in the nucleus, while a decline in expression was noted in the Str-IO group. The AUROC for diagnosing strangulation based on positive and low-positive TNF-α expression in the nucleus was 0.688 (95 % CI 0.410–0.965) and 0.984 (95 % CI 0.936–1.000), respectively, as shown in Fig. 9G. Furthermore, when the Youden index was maximized, a positive and low-positive expression threshold of

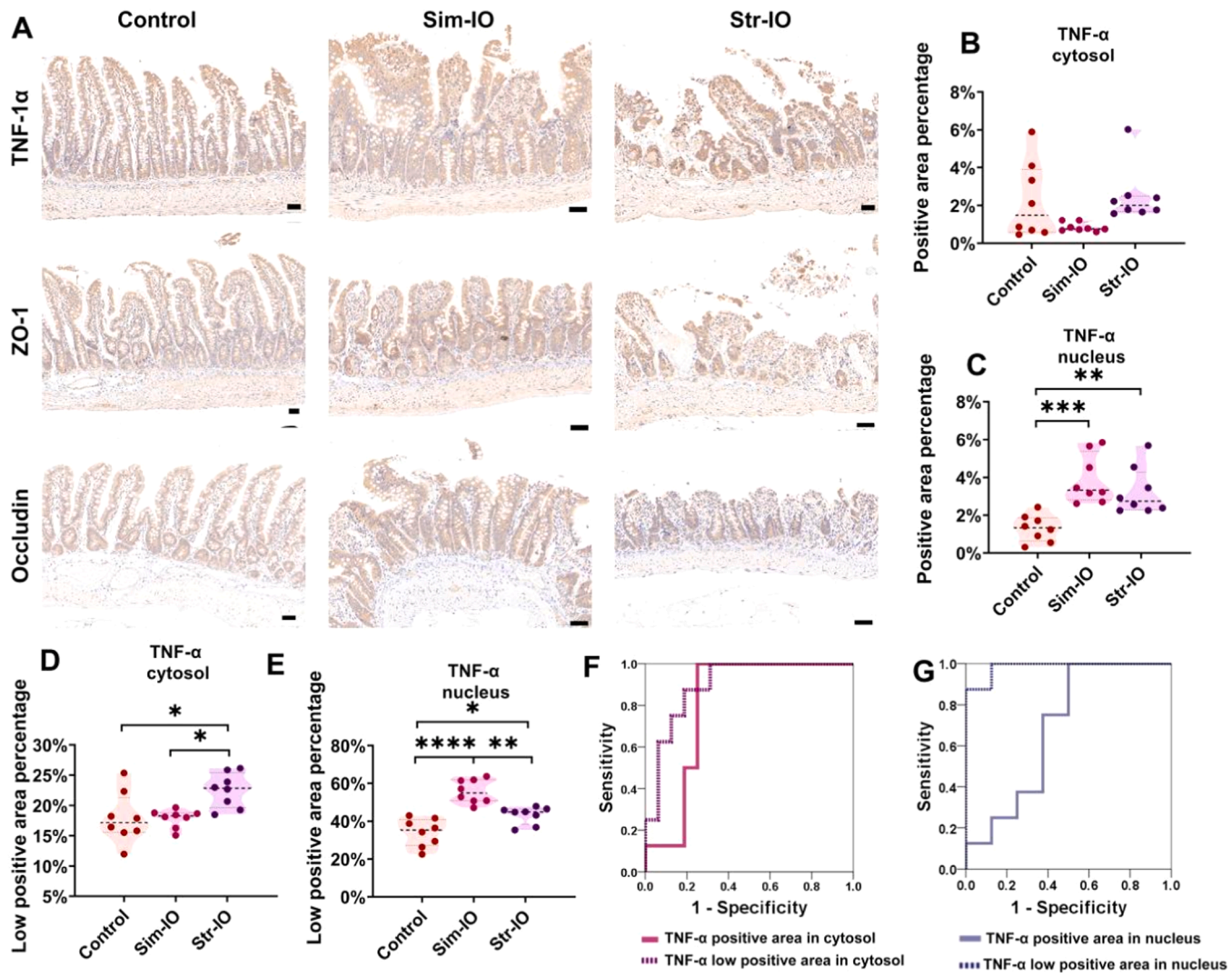

Fig. 9. Correlation analysis of strangulation with inflammation and intestinal barrier function. (A) Expression of TNF-α, ZO-1 and Occludin in Control, Sim-IO and Str-IO group. (B) TNF-α positive area percentage in cytosol, (C) TNF-α positive area percentage in nucleus, (D) TNF-α low positive area percentage in cytosol, (E) TNF-α low positive area percentage in nucleus, (F) ROC curves of TNF-α related parameters in cytosol for diagnosing strangulation. (G) ROC curves of TNF-α related parameters in nucleus for diagnosing strangulation. The date present the mean ± SD ($n = 8$). Comparison among the three groups was performed using one-way ANOVA, with post-hoc pairwise comparisons conducted using Turkey's multiple comparisons test. The black bar representing the length of 50 μm. *$P < 0.05$, * *$P < 0.01$, * **$P < 0.001$, * ** *$P < 0.0001$.

≤ 2.58 % resulted in a sensitivity of 100 % and a specificity of 50 %. In the case of low-positive expression, a threshold of ≤ 48.90 % yielded a sensitivity of 100 % and a specificity of 87.5 %.

3.6. The efficacy of molecular markers in diagnosing strangulation

Molecular markers assessed included L-LA, indicative of intestinal ischemia; MDA, reflective of oxidative stress levels; DAO, associated with intestinal barrier function and integrity; and SOD, representing antioxidant capacity. These biomarkers are widely employed molecular indicators for the assessment of strangulation.

Measurements for L-LA in the Control, Sim-IO, and Str-IO groups were 0.145 ± 0.048, 0.161 ± 0.020, and 0.198 ± 0.040 μmol/L, respectively, with a statistically significant difference observed between the Control and Str-IO groups ($P = 0.0288$). No significant differences were found among the other groups ($P > 0.05$). Results are presented in Fig. 10A (left panel), with the standard curve for L-LA shown on the right ($R^2 = 1.00$).

Regarding MDA, the concentrations for the Control, Sim-IO, and Str-IO groups were 2.76 ± 0.28, 2.22 ± 0.45, and 1.53 ± 0.56 nmol/mL, respectively. A statistically significant difference was noted between the Control and Str-IO groups ($P = 0.0028$), as well as between Sim-IO and Str-IO ($P = 0.0308$). However, no significant difference was observed between the Control and Sim-IO groups ($P = 0.2338$), as illustrated in Fig. 10B.

DAO activity was assessed in the Control, Sim-IO, and Str-IO groups (Fig. 10C), yielding values of 0.05 ± 0.01, 0.05 ± 0.01, and 0.40 ± 0.33 U/mL, respectively. No statistically significant differences were observed among the groups ($P > 0.05$). Similarly, SOD activity in the Control, Sim-IO, and Str-IO groups was measured at 2.16 ± 0.40, 1.29 ± 0.32, and 1.45 ± 0.67 U/mL (Fig. 10D), respectively, with no statistically significant differences identified ($P > 0.05$).

The ROC curves for L-LA, MDA, DAO, and SOD in the diagnosis of strangulation are illustrated in Fig. 8E. The AUROC values were determined to be 0.917 (95 % CI 0.784–1.000), 0.897 (95 % CI 0.765–1.000), 0.650 (95 % CI 0.272–1.000), and 0.075 (95 % CI 0.000–0.216), respectively, with L-LA and MDA demonstrating the highest AUROC values. For L-LA, a threshold of ≥ 0.170 μmol/L yielded the maximum Youden's index, resulting in a sensitivity of 100 % and a specificity of 77.8 % for the diagnosis of strangulation. For MDA, a cutoff of ≤ 1.532

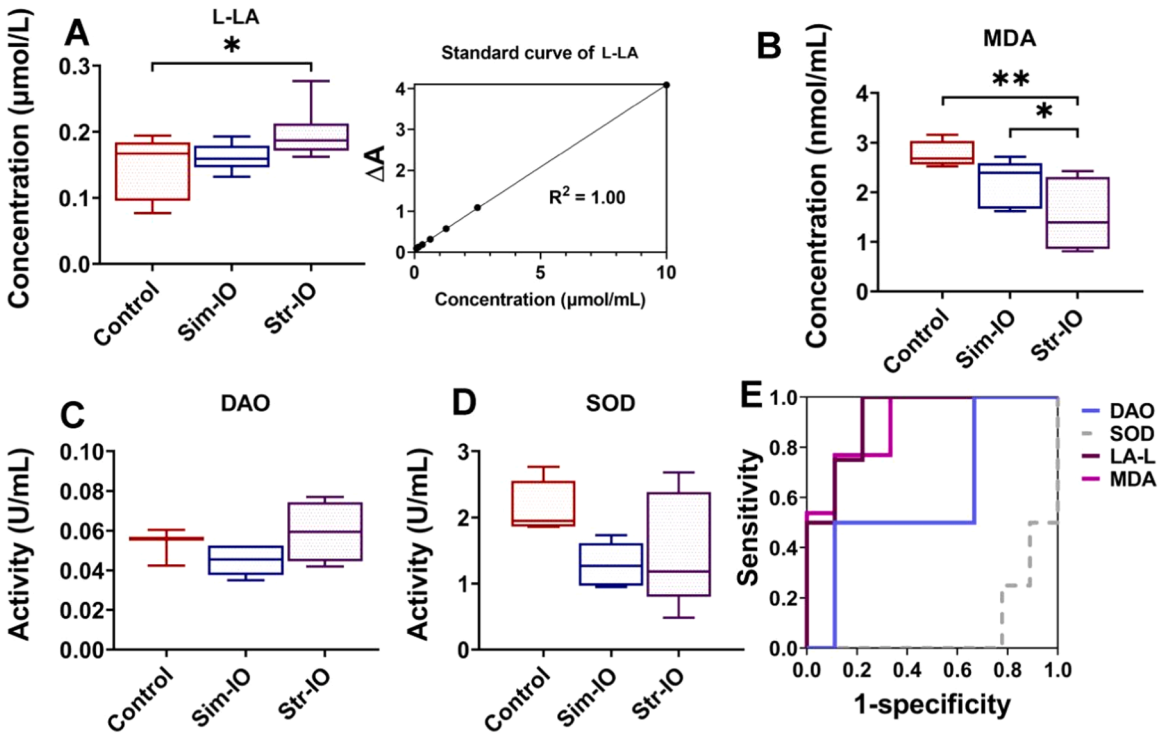

Fig. 10. Molecular markers in Control, Sim-IO, and Str-IO groups and their diagnostic performance in strangulation. (A) Left: concentrations of L-LA in Control, Sim-IO, and Str-IO; Right: standard Curve of L-LA. (B) Concentrations of MDA, (C) DAO and (D) SOD in Control, Sim-IO, and Str-IO. (E) ROC curve of molecular markers in diagnosis strangulation. The date present the mean ± SD ($n = 8$). Comparison among the three groups was performed using one-way ANOVA, with post-hoc pairwise comparisons conducted using Turkey's multiple comparisons test. *$P < 0.05$.

nmol/L also achieved the maximum Youden's index, providing a sensitivity of 100 % and a specificity of 66.7 % for diagnosing strangulation.

4. Discussion

In the context of surgery for acute IO, most patients are unable to ascertain the precise duration of the obstruction. Moreover, relieving the obstruction carries the risk of intestinal ischemia-reperfusion injury, which can result in systemic multi-organ failure, shock, and death. Consequently, although reluctantly acknowledged, most gastrointestinal surgeons follow the principle: "It is better to mistakenly sacrifice three thousand than to let one escape." When diagnostic adjuncts and empirical assessment fail to adequately determine intestinal viability, surgeons typically opt for intestinal resection.

The average length of the small intestine in a normal adult ranges from 5 to 7 m, with some measurements reaching up to 10 m. While the small intestine appears to have a sufficient length reserve, the extent of resection should be carefully considered based on the clinical context. For example, when the diseased segment does not involve the ileocecal region, a longer segment may be resected. However, when the diseased segment includes the ileocecal area and requires its resection, it is essential to preserve as much intestinal length as possible to reduce potential post-operative complications such as malabsorption and steatorrhea. Moreover, in patients with a history of prior intestinal resections, preserving bowel length becomes even more critical to prevent short bowel syndrome.

Empirical judgments and gross scoring by surgeons effectively distinguish between normal and strangulated bowel. However, in cases of Sim-IO, both surgeons exhibited hesitation and inconsistency. As shown in Fig. 7B, in the Sim-IO group, Surgeon 1 classified 75 % of cases as indeterminate, with 25 % identified as strangulation. In contrast, Surgeon 2 assessed 60 % as indeterminate and 40 % as necrotic. These findings emphasize that the greatest challenge in the Sim-IO group lies in the uncertainty of diagnostic judgments, even in the absence of mesenteric strangulation. According to established human treatment guidelines, bowel resection is unnecessary for a blockage lasting 1 hour. Nevertheless, in this study on Sim-IO, when the duration of obstruction was unknown, clinicians estimated that 40 % and 30 % of obstructed animal bowel segments were necrotic and required resection, respectively. It is crucial to recognize that animal models do not fully replicate the complexities of human acute intestinal obstruction, which can further complicate the decision-making process.

Diagnosing IO presents significant challenges, even when combined with imaging methods, laboratory analyses, and the clinical judgment of experienced surgeons. As early as 2005, Hata et al. assessed bowel ischemia using the polymer microbubble SHU-508A via CEUS, demonstrating a sensitivity of 85 % and specificity of 100 %, indicating the potential of CEUS for the noninvasive diagnosis of intestinal ischemia [26]. Subsequently, Sriharsha et al. used DEFINITY® microbubbles (Lantheus Medical Imaging Inc., USA) for CEUS in patients identified by the clinical surgical team as having concerns about small bowel ischemia. The diagnostic sensitivity was 100 %, with a specificity of 85.7 %. In cases where CT suggested small bowel obstruction, CEUS accurately ruled out ischemia in 91.7 % of cases, with a 60 % surgical intervention rate [27]. In terms of CEUS imaging characteristics, intestinal ischemia was observed to present as delayed enhancement, similar to the findings of this study using Sonovue for CEUS. In the case of Str-IO, concurrent blood flow impairment during IO resulted in the lowest PKI and AUC. Although Sim-IO was characterized by an unobstructed mesenteric vascular supply, it was potentially influenced by factors such as intestinal distension and fluid accumulation. These factors can lead to increased intraluminal pressure, obstructing venous return from the bowel wall, thus causing ischemic edema. Consequently, the PKI and AUC values were lower than those of the Control group but higher than those seen in Str-IO. In this study, the diagnostic efficacy of PKI and AUC for detecting IO was found to be high, with AUROC values of 0.995 and 0.979, respectively. Due to its high temporal resolution and

immediate results, CEUS offers unique value in assessing intestinal ischemia. Despite its superior diagnostic performance in this and other studies, CEUS's widespread clinical application remains limited. This limitation is due to the need for additional contrast agent injections and ultrasound systems equipped with contrast capabilities, complicating intraoperative procedures. Furthermore, in the presence of arterial embolism, the use of contrast agents in CEUS may be significantly hindered. In such cases, while tissue ischemia can be assessed, tissue viability remains undetermined.

Most contrast agents approved for ultrasound imaging are blood pool agents, whose micron size prevents them from crossing endothelial cells into surrounding tissues, primarily reflecting blood perfusion rather than tissue oxygenation in CEUS [28]. However, it is important to recognize that blood perfusion and tissue oxygenation, while related, are distinct. Several clinical scenarios may arise in the context of IO [29]: in the initial phase of simple IO, the obstructed and distended bowel causes fluid accumulation within the lumen, leading to increased intraluminal hydrostatic pressure. This pressure compresses capillaries and small venules, disrupting Starling forces that regulate capillary exchange. As a result, there is a significant rise in the net filtration of fluids, electrolytes, and proteins into the bowel wall and lumen. Progressing venous hypertension and ischemia may lead to arterial occlusion, further exacerbating microvascular ischemia. In the strangulated phase of obstruction, both perfusion and oxygenation are severely compromised. Finally, during the ischemia-reperfusion injury phase, perfusion may be restored, but oxygenation remains insufficient. These pathophysiological alterations form the basis for the advancement of CEUS and PA in diagnosing IO. Notably, variations in oxygenation appear to more effectively distinguish the stages of bowel obstruction.

Hemoglobin is an excellent endogenous chromophore. Its unique spectral characteristics, stemming from HBO_2 and HB, enable the extraction of tissue SO_2 from photoacoustic imaging using spectral techniques, eliminating the need for exogenous contrast agents. Significant research has focused on the application of PAT for evaluating inflammation in gastrointestinal diseases, particularly Crohn's disease [15,30,31], employing quantitative hemoglobin content as a metric for inflammation. Additionally, SO_2 serves as a direct measure of tissue oxygen saturation, offering diagnostic value in assessing ischemic regions and the severity of ischemia across various conditions [32–34].

In clinical practice, whether acute mesenteric ischemia, mechanical bowel obstruction, or other forms of IO, the mesenteric vasculature often exhibits compensatory mechanisms to maintain blood supply [35]. As a result, the extent of ischemia and strangulation in the affected bowel segment varies significantly, depending on the severity of ischemia and the degree of compensatory perfusion. Thus, the management of IO requires a holistic evaluation. In this regard, dual-modality US/PAT imaging, which enables precise anatomical localization, comprehensive scanning, and three-dimensional reconstruction, provides a superior diagnostic approach compared to standalone PA or PAT imaging techniques.

The application of dual-modality US/PAT imaging in intestinal assessment remains limited, primarily due to challenges such as imaging depth and interference from intestinal gas. However, under specific conditions, these obstacles may be overcome. For example, during surgery, a PAT probe can be directly placed in segments of the intestine. In a study by Kathryn J et al., PA microscopy was used during extensive small bowel resection to image the microvascular system in real time and measure SO_2 [36]. Furthermore, in cases such as those simulated in this hernia study, where the affected intestine lies just beneath the skin, deep imaging depth is unnecessary [37–39].

SO_2 levels in gross intestinal specimens are generally reported to be low. For instance, a study by Weis et al. found that in a necrotizing enterocolitis (NEC) rat model, intestinal tissue oxygenation averaged 55.90 % ± 3.77 % in the healthy control group, compared to 44.12 % ± 7.18 % in the NEC group [40]. In ischemic and hypoxic states, the body prioritizes blood flow to essential organs, leading to compromised perfusion of non-essential tissues, such as the gastrointestinal tract [41]. As a result, the intestinal epithelium, with its specialized vascular supply and high metabolic demand, becomes particularly susceptible to hypo-perfusion [42].

In this study, although a declining trend in SO_2 levels was observed in the Control, Sim-IO, and Str-IO groups, no statistically significant differences were found ($P = 0.728$). This lack of difference may be due to the inherent hypoxic sensitivity of intestinal tissue, which varies across different animal models. Additionally, under hypoxic conditions, the accumulation of cellular metabolites can induce vascular smooth muscle relaxation, increasing blood flow to hypoxic tissues, which partially compensates for the low tissue SO_2 levels. Further analysis showed that, when examining the frequency distribution of SO_2 across all intestine short axial section, an increase in ischemia severity in the animal models was linked to higher kurtosis, increased skewness. Interestingly, kurtosis and skewness of SO_2 distribution have been underexplored in PAT research. It is suggested that, compared to the Control group, the Sim-IO group exhibited intestinal wall edema, leading to cellular oxygen consumption and the conversion of oxyhemoglobin to deoxyhemoglobin, reducing SO_2 and creating a more concentrated distribution. While vasodilation and increased blood flow may occur, this compensatory mechanism seems insufficient to alleviate the hypoxic state. The Str-IO group experienced even more severe hypoxia, compounded by mesenteric vessel ligation, preventing adequate compensation. Consequently, after oxygen depletion in the constricted intestinal segment, tissue strangulation, acidosis, microthrombosis, and the inability of HBO_2 and HB to exchange oxygen occurred, effectively locking the condition in a state of physiological distress. Zhou et al. analyzed a mesenteric ischemia model in New Zealand White rabbits using hyperspectral imaging alongside SO_2 assessment. Their findings showed a median SO_2 of 70.0 % (interquartile range [IQR], 10.1 %) in normal tissue, compared to a median of 49.6 % (IQR, 14.6 %) in ischemic tissue [43]. In comparison, the median SO_2 in normal tissues in this study was slightly lower, likely due to variations in the animal models used. Additionally, hyperspectral imaging, like X-ray imaging, provides only two-dimensional representations, lacking tomographic capabilities for deeper insights. Nonetheless, the median SO_2 in ischemic tissues closely matched the current findings, never reaching critically low levels (e.g., <30 %). Although the distributions for the Sim-IO and Str-IO groups showed a slight left skew, they still adhered to a basic normal distribution, justifying the use of mean ± standard deviation for representation.

The dual-modality US/PAT imaging technique for SO_2 detection overcomes the spatial resolution limitations of traditional PA imaging, which is confined to localized ROIs or single cross-sectional planes. This advancement enables comprehensive three-dimensional quantitative analysis of tissue-wide SO_2 distribution. In this study, we obtained segmental SO_2 data from the affected intestinal segments and analyzed their distribution characteristics, including kurtosis and skewness. The kurtosis of the SO_2 distribution quantifies the spatial heterogeneity of tissue oxygen saturation; a leptokurtic distribution indicates that SO_2 values are highly concentrated around the mean, reflecting minimal differential tissue SO_2, while a platykurtic distribution signifies greater dispersion of SO_2 values, indicative of notable variance within the tissue. Under physiological conditions, hemoglobin resides solely within the circulatory system. During normal perfusion, SO_2 values in regions with high vascular density are anticipated to be elevated relative to those in areas of low vascular density, thereby clarifying the SO_2 distribution within normal tissues and the disparities in SO_2 distribution between normal and ischemic tissues. As indicated by our findings (Fig. 6D), the SO_2 values in the control group adhered to a normal distribution, with a kurtosis of 3.76 ± 0.79. In contrast, the SO_2 distribution within the Sim-IO group exhibited a sharper peak, indicative of higher kurtosis (kurtosis = 21.72 ± 9.15), a trend that was even more pronounced in the Str-IO group (kurtosis = 141.20 ± 138.07). This suggests that with the increasing severity of intestinal ischemia, the differential between

intravascular and extravascular SO_2 levels diminishes, resulting in a lower overall mean SO2 and a more concentrated distribution.

The skewness of SO_2 distribution serves as a compelling indicator of regional disparities in tissue oxygenation saturation. Negative skewness suggests an increased proportion of localized hypoxic regions (e.g., ischemia), while positive skewness indicates a predominance of hyperoxic areas (e.g., congestion or abnormal perfusion). This study analyzed the skewness of SO_2 distribution among groups. Fig. 6E shows the control group's mean skewness at 0.09 ± 0.33, indicating symmetry. The Sim-IO group had a mean skewness of 0.93 ± 1.16, suggesting a slight left concentration. The Str-IO group exhibited a mean skewness of 5.64 ± 4.36, indicating a significant leftward deviation, reflective of hypoxia and ischemia. While the mean SO_2 value represents the central tendency of the overall data, it fails to capture the spatial heterogeneity of blood oxygen saturation within tissues. Skewness, on the other hand, effectively elucidates the asymmetry in SO_2 distribution, thereby revealing the aberrant distribution characteristics of localized hypoxic regions, offering a more accurate reflection of hypoxic conditions than the mean alone. Particularly in cases where tissue oxygenation is uneven, the mean can obscure the existence of localized hypoxia. For instance, severe hypoxia in certain regions may be compensated for by normal or hyperoxic states in other areas, resulting in an average that falls within a normal range. Aligning with our research approach, Navaneetha et al. employed a parameter analogous to SO_2: the peripheral perfusion index (PPI), a non-invasive measurement obtained via pulse oximetry, aimed at assessing the microcirculatory perfusion status of peripheral tissues in normal neonates. Their findings indicated a leftward skewness in the PPI values of newborns [44]. Research by Charlene R. et al. demonstrated that a negative skewness in SpO2 measurements obtained via pulse oximetry in extremely low birth weight infants indicates an increased risk of early onset sepsis (EOS) [45]. These findings suggest that distribution skewness is a sensitive indicator of aberrant local hypoxic areas within tissues, particularly in this study, where no significant differences were observed in the overall mean values.

Currently, tissue SO_2 quantification is primarily achieved through methods such as pulse oximetry and O_2 microelectrode measurements. However, these techniques have notable limitations. Pulse oximetry is most effective in well-vascularized areas with good blood flow, making it sensitive to variations caused by perfusion issues. In contrast, O_2 microelectrode measurements are limited to the area around the electrode tip and require subcutaneous insertion, preventing a comprehensive assessment of overall tissue SO_2 levels. HIF-1 is a transcription factor consisting of two subunits: the inducible HIF-1α subunit and the constitutively expressed HIF-1β subunit [46]. HIF activation is one of the most extensively studied mechanisms supporting the hypoxic response. In the intestinal environment, low oxygen levels induce the expression of several HIF-1α target genes in intestinal epithelial cells (IECs), reduce HIF-1α degradation, and promote its translocation to the nucleus [47]. Therefore, HIF-1α is often used as a sensitive indicator of hypoxia [48]. The expression levels of HIF-1α in both the nuclear and cytoplasmic compartments differed between the Sim-IO and Str-IO groups compared to the Control group, as shown in Fig. 8B-E. Notably, the highest area under the receiver operating characteristic curve (AUROC) was observed for weak positive nuclear expression of HIF-1α (Fig. 8E), with an AUROC of 1.000 and both diagnostic sensitivity and specificity at 100 %. When expression intensity and the percentage area of HIF-1α were adjusted for cell number, as shown in Fig. 8F and G, both metrics effectively distinguished between the Sim-IO and Str-IO groups. These results substantiate the accuracy of our model groups: Control, Sim-IO, and Str-IO. Additionally, we used HIF-1α as a quantitative standard for assessing tissue hypoxia, validating the accuracy of PAT measurements of SO_2, kurtosis, and skewness in evaluating tissue oxygenation. As shown in Fig. 8M and N, there is a strong correlation between PAT kurtosis and HIF-1α expression, with an R^2 value of 0.80, further supporting the reliability of the PAT system.

Additionally, weak positive expression of TNF-α in the nucleus (Fig. 9E) demonstrated the ability to discriminate between the Sim-IO and Str-IO groups. TNF-α expression was highest in the Sim-IO group, while a decline was noted in the Str-IO group, potentially due to tissue strangulation and cell lysis.

IO is often associated with hypoxia and excessive bacterial growth, leading to metabolic alterations. Research has shown that elevated L-LA levels are closely correlated with the severity and prognosis of intestinal obstruction [49]. In this study, an increasing trend in L-lactate levels was observed with the progression of ischemia; however, statistical significance was found only between the control group and the Str-IO group ($P = 0.0228$), with no significant difference between the Sim-IO and Str-IO groups. Additionally, serum MDA, DAO activity, and SOD activity were selected as molecular biomarkers to assess the diagnostic efficacy for strangulated IO. The decision to measure serum rather than tissue fluid was based on the feasibility of preoperative assessments. While intraoperative analyses may offer enhanced accuracy, they are time-consuming, making tissue fluid analyses less optimal. MDA, a product of lipid peroxidation, typically exhibits elevated levels correlated with oxidative stress, particularly in pathological conditions such as intestinal obstruction. Evaluating MDA levels in serum provides insights into the degree of oxidative stress, offering valuable information about the severity and prognosis of intestinal obstruction [50]. In this study, MDA demonstrated strong diagnostic efficacy, with a P value of 0.0028 in distinguishing between the Control and Str-IO groups and a P value of 0.0308 in differentiating Sim-IO from Str-IO. No apparent trends or cutoff values were identified for DAO and SOD.

In contrast, other assessments, including empirical evaluations by surgeons, gross specimen scoring, demonstrated lower diagnostic accuracy. Based on these findings, the measurement of kurtosis and skewness of SO_2 levels derived from US/PAT shows potential for differentiating the degree of ischemia in intestinal obstruction. This information may assist surgeons in determining the necessity for intestinal segment resection during procedures.

5. Conclusion

Given the limited research on diagnosing IO strangulation through US/PAT imaging, this study successfully employed dual-wavelength imaging alongside ultrasound scanning for PAT imaging, data acquisition, analysis, and three-dimensional reconstruction of SO_2. The kurtosis and skewness of SO_2 distribution were identified as effective indicators for differentiating the status of IO strangulation. Compared to CEUS, the diagnostic efficacy of dual-modality US/PAT imaging showed slight superiority while eliminating the need for contrast agents. Furthermore, Dual-modality US/PAT imaging outperformed both surgeons' experiential assessments and laboratory molecular tests such as L-LA. These findings suggest that dual-modality US/PAT imaging is an ideal methodology for diagnosing IO strangulation. Future developments should focus on miniaturization, convenience, and intraoperative applications.

Funding

This work was supported by the National Natural Science Foundation for Young Scholars of China (grant no. 82302199), Key Research and Development Project of Sichuan Science and Technology Plan Projects (grant no. 2023YFG0322), the Young Fund of Sichuan Natural Science Foundation (grant no. 24NSFSC8075), Postdoctor Research Fund of West China Hospital, Sichuan University (grant no. 2024HXBH181), the Medical Research Project of Chengdu Municipal Health Commission (2021017, 2022338) and the National Science Foundation of China (grant no. 82371977, 82071940, 81671702).

CRediT authorship contribution statement

Huang Yijie: Software. **Qiao Shuaiqi:** Data curation, Formal

analysis, Software. **Wang Xichuan:** Investigation. **Yan Binzi:** Data curation, Formal analysis. **Luo Yan:** Conceptualization, Project administration, Supervision, Validation, Writing – review & editing, Funding acquisition. **Huang Lin:** Methodology, Project administration, Validation, Visualization, Writing – review & editing. **Feng Lian:** Software. **Zhou Jie:** Conceptualization, Data curation, Formal analysis, Investigation, Methodology, Visualization, Writing – original draft, Writing – review & editing. **Yuan Bo:** Investigation. **Ou Mengchuan:** Investigation, Methodology, Writing – original draft, Writing – review & editing.

Declaration of Competing Interest

The authors declare that they have no known competing financial interests or personal relationships that could have appeared to influence the work reported in this paper

Acknowledgements

Thanks to the Pathology Department of the Sixth People's Hospital of Chengdu for their contributions to the pathological assessment of this study.

Data availability

Data will be made available on request.

References

[1] D.W. Proctor, R. Goodall, K. Borsky, J.D. Salciccioli, D.C. Marshall, A. Mohamed, et al., Trends in the mortality, incidence, and disability-adjusted life-years of intestinal obstruction and paralytic ileus: observational study of the Global Burden of Disease database, Br. J. Surg. 110 (12) (2023) 1650–1654, https://doi.org/10.1093/bjs/znad232.

[2] L.S. Bizer, R.W. Liebling, H.M. Delany, M.L. Gliedman, Small bowel obstruction: the role of nonoperative treatment in simple intestinal obstruction and predictive criteria for strangulation obstruction, Surgery 89 (4) (1981) 407–413.

[3] E.K. Paulson, W.M. Thompson, Review of small-bowel obstruction: the diagnosis and when to worry, Radiology 275 (2) (2015) 332–342, https://doi.org/10.1148/radiol.15131519.

[4] C. Girlich, E.M. Jung, E. Huber, C. Ott, I. Iesalnieks, A. Schreyer, et al., Comparison between preoperative quantitative assessment of bowel wall vascularization by contrast-enhanced ultrasound and operative macroscopic findings and results of histopathological scoring in Crohn's disease, Ultraschall Med 32 (2) (2011) 154–159, https://doi.org/10.1055/s-0029-1245398.

[5] S. Wang, Y. Zhao, Y. Xu, Recent advances in applications of multimodal ultrasound-guided photoacoustic imaging technology, Vis. Comput. Ind. Biomed. Art. 3 (1) (2020) 24, https://doi.org/10.1186/s42492-020-00061-x.

[6] H.W. Wang, N. Chai, P. Wang, S. Hu, W. Dou, D. Umulis, et al., Label-free bond-selective imaging by listening to vibrationally excited molecules, Phys. Rev. Lett. 106 (23) (2011) 238106, https://doi.org/10.1103/PhysRevLett.106.238106.

[7] V.V. Yakovlev, H.F. Zhang, G.D. Noojin, M.L. Denton, R.J. Thomas, M.O. Scully, Stimulated Raman photoacoustic imaging, Proc. Natl. Acad. Sci. 107 (47) (2010) 20335–20339, https://doi.org/10.1073/pnas.1012432107.

[8] A. de la Zerda, J.W. Kim, E.I. Galanzha, S.S. Gambhir, V.P. Zharov, Advanced contrast nanoagents for photoacoustic molecular imaging, cytometry, blood test and photothermal theranostics, Contrast Media Mol. Imaging 6 (5) (2011) 346–369, https://doi.org/10.1002/cmmi.455.

[9] G.C.W. F. Alan McDonald, Generalized theory of the photoacoustic effect, J. Appl. Phys. 49 (4) (1978) 2313–2322, https://doi.org/10.1063/1.325116.

[10] L.V. Wang, J. Yao, A practical guide to photoacoustic tomography in the life sciences, Nat. Methods 13 (8) (2016) 627–638, https://doi.org/10.1038/nmeth.3925.

[11] W. Choi, B. Park, S. Choi, D. Oh, J. Kim, C. Kim, Recent advances in contrast-enhanced photoacoustic imaging: overcoming the physical and practical challenges, Chem. Rev. 123 (11) (2023) 7379–7419, https://doi.org/10.1021/acs.chemrev.2c00627.

[12] H. Liu, X. Teng, S. Yu, W. Yang, T. Kong, T. Liu, Recent advances in photoacoustic imaging: current status and future perspectives, Micromachines 15 (8) (2024), https://doi.org/10.3390/mi15081007.

[13] A. Attia, G. Balasundaram, M. Moothanchery, U.S. Dinish, R. Bi, V. Ntziachristos, et al., A review of clinical photoacoustic imaging: current and future trends, Photoacoustics 16 (2019) 100144, https://doi.org/10.1016/j.pacs.2019.100144.

[14] G. Yang, E. Amidi, W. Chapman, S. Nandy, A. Mostafa, H. Abdelal, et al., Co-registered photoacoustic and ultrasound imaging of human colorectal cancer, J. Biomed. Opt. 24 (12) (2019) 1–13, https://doi.org/10.1117/1.JBO.24.12.121913.

[15] F. Knieling, C. Neufert, A. Hartmann, J. Claussen, A. Urich, C. Egger, et al., Multispectral optoacoustic tomography for assessment of crohn's disease activity, N. Engl. J. Med. 376 (13) (2017) 1292–1294, https://doi.org/10.1056/NEJMc1612455.

[16] A. Buehler, E. Brown, L.P. Paulus, M. Eckstein, O.M. Thoma, M.E. Oraiopoulou, et al., Transrectal absorber guide raster-scanning optoacoustic mesoscopy for label-free in vivo assessment of colitis, Adv. Sci. 10 (18) (2023) e2300564, https://doi.org/10.1002/advs.202300564.

[17] A. Buehler, E.L. Brown, E. Nedoschill, M. Eckstein, P. Ludwig, F. Wachter, et al., In vivo assessment of deep vascular patterns in murine colitis using optoacoustic mesoscopic imaging, Adv. Sci. (2024) e2404618, https://doi.org/10.1002/advs.202404618.

[18] W. Huang, R. Chen, Y. Peng, F. Duan, Y. Huang, W. Guo, et al., In vivo quantitative photoacoustic diagnosis of gastric and intestinal dysfunctions with a broad ph-responsive sensor, Acs Nano 13 (8) (2019) 9561–9570, https://doi.org/10.1021/acsnano.9b04541.

[19] R. Wang, T. Pan, L. Huang, C. Liao, Q. Li, H. Jiang, et al., Photoacoustic imaging in evaluating early intestinal ischemia injury and reperfusion injury in rat models, Quant. Imaging Med. Surg. 11 (7) (2021) 2968–2979, https://doi.org/10.21037/qims-20-1160.

[20] T. Sugiura, K. Okumura, J. Matsumoto, M. Sakaguchi, T. Komori, T. Ogi, et al., Predicting intestinal viability by consecutive photoacoustic monitoring of oxygenation recovery after reperfusion in acute mesenteric ischemia in rats, Sci. Rep. 11 (1) (2021) 19474, https://doi.org/10.1038/s41598-021-98904-x.

[21] C. Li, L.V. Wang, Photoacoustic tomography and sensing in biomedicine, Phys. Med. Biol. 54 (19) (2009) R59–R97, https://doi.org/10.1088/0031-9155/54/19/R01.

[22] C.J. Chiu, A.H. McArdle, R. Brown, H.J. Scott, F.N. Gurd, Intestinal mucosal lesion in low-flow states. I. A morphological, hemodynamic, and metabolic reappraisal, Arch. Surg. 101 (4) (1970) 478–483, https://doi.org/10.1001/archsurg.1970.01340280030009.

[23] F. Varghese, A.B. Bukhari, R. Malhotra, A. De, IHC Profiler: an open source plugin for the quantitative evaluation and automated scoring of immunohistochemistry images of human tissue samples, Plos One 9 (5) (2014) e96801, https://doi.org/10.1371/journal.pone.0096801.

[24] D.K. Cowden, B.H. Fryer, F.A. Mack, V. Compernolle, E. Maltepe, D.M. Adelman, et al., Hypoxia-inducible factors 1alpha and 2alpha regulate trophoblast differentiation, Mol. Cell. Biol. 25 (23) (2005) 10479–10491, https://doi.org/10.1128/MCB.25.23.10479-10491.2005.

[25] W. Qi, M. Zhuo, Y. Tian, Z. Dawa, J. Bao, Y. An, Application of Intelligent Monitoring of Percutaneous Partial Oxygen Pressure in Evaluating the Evolution of Scar Hyperplasia, J. Healthc. Eng. 2021 (2021) 8241193, https://doi.org/10.1155/2021/8241193.

[26] J. Hata, T. Kamada, K. Haruma, H. Kusunoki, Evaluation of bowel ischemia with contrast-enhanced US: initial experience, Radiology 236 (2) (2005) 712–715, https://doi.org/10.1148/radiol.2362040299.

[27] S. Gummadi, G. Koenig, C.E. Wessner, P. Machado, J. Stem, F. Forsberg, et al., Contrast-Enhanced Ultrasound in Small Intestinal Ischemia: proof of Concept, J. Ultrasound Med. 41 (4) (2022) 835–843, https://doi.org/10.1002/jum.15763.

[28] S.R. Wilson, P.N. Burns, Microbubble-enhanced US in body imaging: what role? Radiology 257 (1) (2010) 24–39, https://doi.org/10.1148/radiol.10091210.

[29] A.J. Hayanga, K. Bass-Wilkins, G.B. Bulkley, Current management of small-bowel obstruction, Adv. Surg. 39 (2005) 1–33, https://doi.org/10.1016/j.yasu.2005.05.001.

[30] H. Lei, L.A. Johnson, S. Liu, D.S. Moons, T. Ma, Q. Zhou, et al., Characterizing intestinal inflammation and fibrosis in Crohn's disease by photoacoustic imaging: feasibility study, Biomed. Opt. Express 7 (7) (2016) 2837–2848, https://doi.org/10.1364/BOE.7.002837.

[31] N. Bhutiani, W.E. Grizzle, S. Galandiuk, D. Otali, G.W. Dryden, N.K. Egilmez, et al., Noninvasive imaging of colitis using multispectral optoacoustic tomography, J. Nucl. Med. 58 (6) (2017) 1009–1012, https://doi.org/10.2967/jnumed.116.184705.

[32] B. Park, D. Oh, J. Kim, C. Kim, Functional photoacoustic imaging: from nano- and micro- to macro-scale, Nano Converg. 10 (1) (2023) 29, https://doi.org/10.1186/s40580-023-00377-3.

[33] Q. Yang, L. Yang, C. Peng, X. Zhu, Z. Wu, L. Huang, et al., Testicular torsion diagnosis and injury assessment using photoacoustic oxygenation imaging, Photoacoustics 31 (2023) 100499, https://doi.org/10.1016/j.pacs.2023.100499.

[34] A. Dima, J. Gateau, J. Claussen, D. Wilhelm, V. Ntziachristos, Optoacoustic imaging of blood perfusion: techniques for intraoperative tissue viability

assessment, J. Biophotonics 6 (6-7) (2013) 485–492, https://doi.org/10.1002/jbio.201200201.
[35] L.G. Terlouw, A. Moelker, J. Abrahamsen, S. Acosta, O.J. Bakker, I. Baumgartner, et al., European guidelines on chronic mesenteric ischaemia - joint United European Gastroenterology, European Association for Gastroenterology, Endoscopy and Nutrition, European Society of Gastrointestinal and Abdominal Radiology, Netherlands Association of Hepatogastroenterologists, Hellenic Society of Gastroenterology, Cardiovascular and Interventional Radiological Society of Europe, and Dutch Mesenteric Ischemia Study group clinical guidelines on the diagnosis and treatment of patients with chronic mesenteric ischaemia, U. Eur. Gastroenterol. J. 8 (4) (2020) 371–395, https://doi.org/10.1177/2050640620916681.
[36] K.J. Rowland, J. Yao, L. Wang, C.R. Erwin, K.I. Maslov, L.V. Wang, et al., Immediate alterations in intestinal oxygen saturation and blood flow after massive small bowel resection as measured by photoacoustic microscopy, J. Pediatr. Surg. 47 (6) (2012) 1143–1149, https://doi.org/10.1016/j.jpedsurg.2012.03.020.
[37] Y. Zhu, L. Ni, G. Hu, L.A. Johnson, K.A. Eaton, X. Wang, et al., Prototype endoscopic photoacoustic-ultrasound balloon catheter for characterizing intestinal obstruction, Biomed. Opt. Express 13 (6) (2022) 3355–3365, https://doi.org/10.1364/BOE.456672.
[38] H. Lei, L.A. Johnson, K.A. Eaton, S. Liu, J. Ni, X. Wang, et al., Characterizing intestinal strictures of Crohn's disease in vivo by endoscopic photoacoustic imaging, Biomed. Opt. Express 10 (5) (2019) 2542–2555, https://doi.org/10.1364/BOE.10.002542.
[39] K. Xiong, S. Yang, X. Li, D. Xing, Autofocusing optical-resolution photoacoustic endoscopy, Opt. Lett. 43 (8) (2018) 1846–1849, https://doi.org/10.1364/OL.43.001846.
[40] J.A. Weis, J.L. Rauh, M.A. Ellison, N. Cruz-Diaz, L.M. Yamaleyeva, C.D. Welch, et al., Photoacoustic Imaging for non-invasive assessment of physiological biomarkers of intestinal injury in experimental necrotizing enterocolitis, Biorxiv (2023), https://doi.org/10.1101/2023.10.20.563296.
[41] W. He, Y. Wang, P. Wang, F. Wang, Intestinal barrier dysfunction in severe burn injury, Burns Trauma 7 (2019) 24, https://doi.org/10.1186/s41038-019-0162-3.
[42] S.P. Colgan, C.T. Taylor, Hypoxia: an alarm signal during intestinal inflammation, Nat. Rev. Gastroenterol. Hepatol. 7 (5) (2010) 281–287, https://doi.org/10.1038/nrgastro.2010.39.
[43] Y. Zhou, L. Zhang, D. Huang, Y. Zhang, L. Zhu, X. Chen, et al., Hyperspectral imaging combined with blood oxygen saturation for in vivo analysis of small intestinal necrosis tissue, Spectroc. Acta Pt. A-Molec. BioMolec. Spectr. 315 (2024) 124298, https://doi.org/10.1016/j.saa.2024.124298.
[44] N. Sasikumar, N.S. Madhavankutty, G. Gutjahr, P. Bendapudi, A. Moosa, K. Prasenan, et al., Distribution and reference values of peripheral perfusion index in neonates from population-wide screening, BMJ Paediatr. Open 8 (1) (2024), https://doi.org/10.1136/bmjpo-2024-002607.
[45] C.R. Bultmann, J. Qiu, B. Belmonte, K.D. Fairchild, B.A. Sullivan, Heart rate and oxygen saturation patterns in very low birth weight infants with early onset sepsis and histologic chorioamnionitis, J. Neonatal Perinat. Med 17 (2) (2024) 209–215, https://doi.org/10.3233/NPM-230093.
[46] G.L. Wang, B.H. Jiang, E.A. Rue, G.L. Semenza, Hypoxia-inducible factor 1 is a basic-helix-loop-helix-PAS heterodimer regulated by cellular O2 tension, Proc. Natl. Acad. Sci. 92 (12) (1995) 5510–5514, https://doi.org/10.1073/pnas.92.12.5510.
[47] L.P. Pral, J.L. Fachi, R.O. Correa, M. Colonna, M. Vinolo, Hypoxia and HIF-1 as key regulators of gut microbiota and host interactions, Trends Immunol. 42 (7) (2021) 604–621, https://doi.org/10.1016/j.it.2021.05.004.
[48] W. Guo, J.M. Feng, L. Yao, L. Sun, G.Q. Zhu, Transplantation of endothelial progenitor cells in treating rats with IgA nephropathy, BMC Nephrol. 15 (2014) 110, https://doi.org/10.1186/1471-2369-15-110.
[49] R. Kintu-Luwaga, M. Galukande, F.N. Owori, Serum lactate and phosphate as biomarkers of intestinal ischemia in a Ugandan tertiary hospital: a cross-sectional study, Int. J. Emerg. Med. 6 (1) (2013) 44, https://doi.org/10.1186/1865-1380-6-44.
[50] A. Ivanov, S. Khinev, G. Koinova, K. Dafinova, The determination of plasma malondialdehyde in patients with obstruction of the small intestine, Khirurgiia 48 (4) (1995) 38–40.

Jie Zhou Postdoctoral researcher and associate researcher in the Ultrasound Department at West China Hospital of Sichuan University. Focuses primarily on ultrasound and photoacoustic imaging research related to abdominal diseases.

Mengchuan Ou Attending Physician in the Gastrointestinal and Vascular Surgery Department at Chengdu Sixth People's Hospital, specializing in clinical diagnosis and innovative treatment methods for gastrointestinal and vascular diseases.

Bo Yuan Associate Chief Physician and Assistant Director of the Gastrointestinal Surgery Department at Chengdu Sixth People's Hospital, specializes in the treatment of gastrointestinal surgical diseases, complex critical surgical cases, and nutritional support.

Binzi Yan Ph.D. candidate of the West China Clinical Medicine College, Sichuan University, with a primary research focus on ultrasound diagnosis of abdominal diseases.

Xichuan Wang Chief Physician and Director of the Pathology Department at Chengdu Sixth People's Hospital, has engaged in clinical pathological diagnosis for nearly 30 years. Specializes in pathological diagnosis across various system diseases, with particular expertise in digestive system disorders.

Shuaiqi Qiao Master's student in Electronic Science and Technology at University of Electronic Science and Technology of China, with a primary research focus on optical information science and technology.

Yijie Huang born in Sichuan, China, in 2000, received a B.S. degree from the University of Electronic Science and Technology of China (UESTC) in Chengdu in 2022. Currently pursuing a Ph.D. degree at the School of Electronic Science and Engineering at UESTC, Yijie is also affiliated with Zhangjiang Laboratory in Shanghai, China. Research interests are concentrated on electromagnetic-acoustic imaging.

Lian Feng Ph.D. candidate at West China School of Medicine, Sichuan University, focuses on ultrasound imaging algorithms, signal processing, and photoacoustic/thermoacoustic imaging technologies.

Lin Huang Associate Professor and Master's supervisor at the University of Electronic Science and Technology, is affiliated with the Sichuan Advanced Optoelectronic Integrated RF Metamaterial Chip Engineering Center. As a member of the China Institute of Electronics, serves as Guest Editor for Photonics special issue "Advances in Biophotonics" and Guest Associate Editor for Frontiers in Physics. Focused on interdisciplinary research at the intersection of electromagnetic-acoustic imaging, sensing technologies, and life sciences, current projects include microwave thermoacoustics, terahertz acoustics, and photoacoustic imaging for applications in disease detection, intraoperative guidance, efficacy evaluation, and multi-physical therapies. Leadership roles encompass the National Natural Science Foundation of China's Youth Program, the JKW Frontier Exploration Program, and key R&D initiatives in Sichuan province, along with participation in several national major projects. With over 40 publications in prestigious journals such as Photoacoustics, APL, Medical Physics, Science Advances, IEEE Transactions on Biomedical Engineering, and IEEE Transactions on Terahertz Science and Technology, contributions also include the translation of Photoacoustic Imaging, enhancing knowledge in this emerging field.

Yan Luo Professor and chief physician in the Department of Ultrasound of West China Hospital, Sichuan University, and a leading figure in academic and technical fields within Sichuan Province. Currently serving as the head of the Department of Ultrasound and the director of the West China Thomas Jefferson Ultrasound Education Sub-center, Luo also holds the position of deputy director of the Medical Imaging Center. The primary focus of research encompasses abdominal ultrasounds, particularly in relation to liver diseases, alongside foundational studies in engineering and medical applications, including signal processing, image reconstruction, data analysis, and emerging imaging technologies.